Spacecraft Attitude Control by Magnetic Actuation and Double-Gimbal Variable-Speed Control Moment Gyroscope

Andrew Francesco Taddio Ilersich
1001247965

Supervised by Professor Christopher J. Damaren

A thesis submitted in conformity with the requirements
for the degree of Bachelor of Applied Science, Aerospace
Division of Engineering Science
University of Toronto

Abstract

Magnetic attitude control systems are extremely common for small satellites due to their simplicity, low cost, and compactness. They however lack a degree of freedom: they cannot apply torque about a magnetic field line. This thesis proposes a hybrid attitude control system consisting of one double-gimbal variable-speed control moment gyroscope and three orthogonal magnetic torque actuators. The VSCMG is chosen to make up for the lost degree of freedom with minimal hardware. The dynamics equations are derived then control laws are proposed and analyzed for cases of detumbling the spacecraft and holding it at a given attitude. The performance characteristics are analyzed with respect to the control gains for each actuator type and optimal ratios of the two are identified. This hybrid system is shown to have better convergence time in detumbling and precision in attitude holding than a purely magnetic system.

Acknowledgements

I would like to thank Professor Damaren for his meticulous and patient guidance over the past year. He took the time to walk me through so much when he could have far more easily referred me to a textbook, he caught mistakes that might have otherwise made their way into the final document, and he always made time for discussion when he was otherwise very busy. If not for his mentorship, my thesis would not contain the depth and polish that it does.

I would also like to thank my parents for their endless support. When I was focusing more and more on studies and putting everything else on hold, they were there to give me fresh food, to drive me to and from campus, and to make sure I didn't forget anyone's birthday. I'm reminded how lucky I am every time I have to convince them that I don't mind taking public transit instead of getting driven.

Contents

List of Figures

List of Acronyms

ACS Attitude Control System

RCS Reaction Control System (used here to refer to impulsive thruster systems)

GGS Gravity Gradient Stabilization

CMG Control Moment Gyroscope

VSCMG Variable-Speed Control Moment Gyroscope

MTA Magnetic Torque Actuator

RCW Reaction Control Wheel

EMI Electro-Magnetic Interference

LQR Linear Quadratic Regulator

PID Proportional-Integral-Derivative

List of Variables

μ Gravitational constant $\times$ mass of Earth
n Orbital frequency around Earth at a given altitude
ϕ Orbit inclination
R Orbit radius (distance to centre of Earth)
$\boldsymbol{p_i}, \boldsymbol{p_b}$ Spacecraft position in orbit in inertial/body frames
$\boldsymbol{R_b^i}$ Rotation matrix from inertial frame to spacecraft body frame
B_0 Strength of Earth's magnetic field
$\boldsymbol{B_i}, \boldsymbol{B_b}$ Magnetic field from Earth in inertial/body frames

$\boldsymbol{I_{sat}}$ Moment of inertia matrix for whole spacecraft
γ_o Outer gimbal carriage angle
γ_i Inner gimbal carriage angle
Ω_g Scalar angular rate of flywheel (can apply to RCW or VSCMG)
$\boldsymbol{\alpha_g}$ Angular acceleration of flywheel (can apply to RCW or VSCMG)
I_g Moment of inertia about spinning axis for flywheel (can apply to RCW or VSCMG)
$\boldsymbol{m}$ Magnetic dipole moment applied by MTAs

$\boldsymbol{q}$ Orientation of spacecraft (quaternion)
  η Scalar component of quaternion
  $\boldsymbol{\epsilon}$ Vector component of quaternion
$\boldsymbol{\omega}$ Angular velocity of spacecraft
$\boldsymbol{c}$ VSCMG state vector $= \begin{bmatrix} \gamma_o & \gamma_i & \Omega_g \end{bmatrix}^T$

Note: the same vector in different reference frames is only rotated, not translated. Hence $\boldsymbol{p}_b$ is not a zero vector.

Introduction

Attitude control for spacecraft usually requires a relatively large, expensive system to perform. In most large spacecraft, including the Space Shuttle [1], this is done with a monopropellant or cold gas thruster reaction control system, which require careful positioning, a structure to distribute the force on the frame, and large propellant tanks that pose a safety hazard and change the mass distribution as they are used up. An alternative is reaction control wheels (RCW), which have the advantage of being mounted internally and conserving energy, but can be saturated and require a carefully-fabricated low-friction environment to function. More recently, low-cost satellites, especially those following the "cubesat" standard, have taken advantage of the magnetic field of earth for attitude control.[5] Electromagnetic torquers are precisely controllable, have no moving parts, and can be mounted internally like RCW. They however have one major drawback. From the cross product for torque:

$$\vec{\tau}_{mta} = \vec{m} \times \vec{B} = \vec{\mathcal{F}}_b \boldsymbol{m}^{\times} \boldsymbol{B}_b \tag{1}$$

The torque vector $\vec{\tau}$ will always be orthogonal to the magnetic field line $\vec{B}$, hence there is one rotational axis that magnetic torquers will always lack. This can be solved by acting on perturbations in the magnetic field, but this would mean waiting for certain opportune positions in the orbital path. Other alternatives involve combining magnetic torquers with RCWs or traditional thrusters, which have been well studied by my supervisor, Professor Damaren.[8][26] This however provides redundant degrees of freedom.

The solution that I am investigating is combining the magnetic torquers with a variable-speed control moment gyroscope (VSCMG) mounted inside a two-axis gimbal. I am investigating the dynamics and control laws governing this system and its efficiency compared to other arrangements of attitude control systems. The dynamic equations will be derived assuming a spacecraft of known geometry and mass and conserved angular momentum. The first stage of control law testing is for detumbling, followed by full attitude control via proportional derivative feedback. The VSCMG component will be linearized for ease of analysis and complemented with numerical simulations.

Chapter 1

Background

1.1 ACS Mechanisms

For most spacecraft orbiting the Earth, there are five main options for an Attitude Control System (ACS). These are impulsive thrusters in a Reaction Control System (RCS), Gravity Gradient Stabilization (GGS), Reaction Control Wheels (RCW), Magnetic Torque Actuators (MTA), and Control Moment Gyroscopes (CMG), which further divide into constant speed and variable speed versions.

An impulsive thruster RCS is common on large spacecraft like the Space Shuttle [1] with high moments of inertia and where fuel is more abundant. These systems are arrangements of thrusters around a spacecraft offset from the centre of mass. To get the spacecraft to rotate, pairs of opposed thrusters will fire at the same time and throttle so that there is no net translational force on the spacecraft. These systems are relatively large and complicated compared to the other systems discussed here and require the most structural accommodation. They also require an onboard supply of mass to eject, thus they cannot be recharged indefinitely with a solar panel. For these reasons, these systems are not found on small spacecraft.

GGS takes advantage of the fact that gravity is weaker with greater altitude. The near side of the spacecraft is being pulled on with stronger gravity than the far side, applying a torque that keeps the same side facing the Earth. The greater asymmetry between principal axes' moments of inertia, the stronger this effect. Like the RCS, this has been used with larger spacecraft, such as the Salyut-Soyuz orbital complex [22]. In order to augment the effect, many spacecraft designed to use GGS will feature a long weighted boom arm. The torque applied is given by Equation 1.1 [26].

$$\vec{\tau}_{ggs} = \vec{\mathcal{F}}_b \frac{3\mu}{R^5} \boldsymbol{p}_b^{\times} \boldsymbol{I}_{sat} \boldsymbol{p}_b \tag{1.1}$$

The RCW consists simply of a motorized heavy flywheel. By conservation of angular momentum, accelerating the flywheel applies a torque to the spacecraft in the opposite direction. In their prototypical configuration, three RCWs are mounted on orthogonal axes so that a spacecraft has full attitude control. Due to their simplicity, they are common on smaller and lower-cost spacecraft, especially cubesats. A drawback however is that these wheels cannot spin infinitely fast; at some point the RCW reaches its maximum speed (i.e. is 'saturated') and the ACS then loses that degree of freedom. This can happen in very long-term missions where the net torque over time from the environment is nonzero. In most spacecraft, this is usually due to gravity gradient effects. For a single RCW, the torque applied is given in Equation 1.2.

$$\vec{\tau}_{rcw} = \vec{\mathcal{F}}_b I_g \boldsymbol{\alpha}_g \tag{1.2}$$

There are two common configurations of CMG. The simplest type is the single-gimbal CMG, where a motorized gyroscope is placed inside a gimbal carriage. This carriage rotates on an axis orthogonal to the gyro axis. A more complicated version of CMG is the double-gimbal type, where there are two carriages with initially orthogonal rotary axes. The CMG applies a gyroscopic torque when a gimbal carriage rotates, and this torque is is proportional to both the angular speeds of the gyro and of the gimbal carriage. The gyro may be either fixed or variable speed; Section 2.2.1 presents the variable speed version dynamics in detail. For the fixed speed version, the dynamics can be obtained by setting $\dot{\Omega}_g = 0$.

Only the double-gimbal VSCMG configuration provides the full three degrees of freedom. Other versions of CMG must be used in arrangements of more than one in order to obtain full attitude control. Whatever the type or arrangement of CMG, it can saturate when it reaches a position called "gimbal lock", where enough control axes are parallel such that a degree of freedom is lost. In the case of a double-gimbal VSCMG, this is where the gyro axis is parallel to a gimbal axis. Like with RCWs, this can occur on especially long-term missions, but can be delayed by giving the flywheel a higher angular speed, hence requiring less gimbal movement for the same torque. When supplemented with saturation-free actuators like MTAs, gimbal lock can be avoided completely.

MTAs harness Earth's magnetic field for attitude control. They consist of electromagnets fixed to the body of the spacecraft, so that when they are powered they will try to line up with the environmental magnetic field lines. They usually take the form of solenoid electromagnets with a high-permeability core. Like RCWs, they are often in arrangements with three on

orthogonal axes. While these have the benefit of never saturating, they are less effective at more distant orbits and the rest of the spacecraft must be designed to handle the EMI caused by it. They also have the drawback that, since torque applied is the cross product of the MTA's field and the environmental magnetic field vector, the torque axis must lie in the plane that the field vector is normal to. Therefore at any given time, the MTA-equipped spacecraft is lacking a degree of freedom. This is usually managed by taking advantage of the time-varying nature of Earth's magnetic field over the course of an inclined orbit, but MTA control has a fundamental gain restriction to guarantee stability, as detailed in [14]. This limits the convergence time and thus the precision of the ACS. The torque applied by a single MTA is given in Equation 1.

1.2 Brief History of the MTA

One of the earliest studies into the use of MTAs on spacecraft for attitude control was conducted by NASA Ames researchers in 1961.[21] It demonstrated a variation in magnetic field strength with approximately twice orbital frequency, demonstrated two-axis attitude control for the Orbiting Astronomical Observatory within 0.5 μrad, and proposed the MTA as a method of desaturating other actuators in a hybrid system. The B-dot control law, which has become the standard for three-axis MTA systems and is the starting point for MTA control laws considered in this thesis, was first proposed in [4] in 1974. A survey of attitude control by MTAs demonstrated convergence using simulations of different control procedures, including controllers designed using linearized dynamics and the B-dot law.[23] The B-dot law (and its approximation discussed here in Section 3.1.1) was the only nonlinear controller design strategy discussed in the survey.

The Ørsted satellite in 1999 made use of GGS and MTAs in a hybrid system in a mission to study the Earth's magnetic field; the scientific instruments onboard were highly precise magnetometers and a star tracker that were used for both data collection and attitude control. A paper studying this ACS demonstrated detumbling convergence for variable-gain and LQR controllers.[28] The potential for use in microsatellites has been recognized and realized over the past few years especially. A good example is the UPMSAT-2, a technology demonstrator that uses the B-dot law alone for its ACS.[29] The OUFTI-1 and OUFTI-2 cubesats which were deployed in 2016 used MTAs for attitude control. On top of the B-dot and LQR controllers, the paper on OUFTI's attitude control system considered a PID controller based on desired torques, but none of the three produced comparable accuracy to a PD controller for a hybrid system of MTAs and RCWs, which the paper ultimately recommended.[9]

1.3 Brief History of the VSCMG

An early study of the use of CMGs in spacecraft attitude control was conducted by Boeing researchers in 1966.[6] It contained a derivation of the dynamics for both the single and double-gimbal constant-speed versions and demonstrated controllability in an analog computer simulation. Much of the research since then has gone into strategies to avoid the singularities, concerning optimal physical arrangements[2] or initial poisitons.[17] The use of a single double-gimbal VSCMG for attitude control has been proposed before in [12], which proposes and demonstrates stability for the same control law that is used in this paper. More recently there has been interest in CMG clusters for small satellites, demonstrating a potential performance advantage over RCWs for similar size spacecraft.[13]

CMGs were first used on a spacecraft in Skylab in 1973. Three double-gimbal CMGs were mounted with initially orthogonal gyro axes. The range of motion on each gimbal carriage was mechanically limited: the inner gimbal had stops at $\pm 1.4\ rad$ and the outer gimbal had stops at $-2.3\ rad$ and $3.8\ rad$.[3] The control logic was designed to minimize encounters with the gimbal stops, so the CMGs were not as effective as they could have been with a less limited controller. The Mir space station had an array of twelve CMGs, six mounted on each of two modules. These CMGs however were only used for holding a given attitude. When the space station's attitude needed a large adjustment, the CMGs were disabled and impulsive thrusters moved it to the new position.[20] The only current spacecraft that uses CMGs is the ISS, which has an array of four. While this system is also primarily intended for attitude holding rather than adjustment, the space station has performed limited maneuvering using the CMGs. In particular, they have been used during undocking of the Soyuz to save propellant.[25]

1.4 Hybrid Arrangements

ACSs on small satellites, especially those following the cubesat standard, tend to be extremely simple. On a 1U cubesat, the ACS is restricted to $150 - 200\ g$ of mass and $1\ W$ of power consumption. Because space, weight, and power are so limited, simple passive ACS are popular among cubesat designers.[16] Because GGS has a weaker effect on small, symmetric spacecraft, this passive control is most easily accomplished by permanent magnets that make use of the same effect as MTAs. To bridge the gap for these smallest cubesats, there has been successful research into making use of hybrid passive/active magnetic systems for attitude control.[16] Entirely active systems do not become common until we look at larger cubesats.

For medium to large cubesats, the two most common active ACSs are RCWs and MTAs. Damaren has studied the case of combining these two actuators in a hybrid ACS and demonstrated the success of such a method even with fewer than three RCWs available.[1] For larger spacecraft still, where impulsive thrusters are a practical option, Damaren has also studied the hybrid ACS of thrusters and MTAs and, with an optimized linear controller, demonstrated improved performance and reduced MTA effort with missions that require high pointing accuracy.[26]

My thesis is a similar hybrid analysis, where the combination is of three orthogonal MTAs and a VSCMG. Like with RCWs, the MTAs have the ability when properly oriented to desaturate the VSCMG, while the VSCMG can make up for the lost axis of an MTA system and do so in a far shorter convergence time. Like Damaren's work, my thesis attempts to find an optimal combination of the different systems within the hybrid. This is fundamentally different from a superficially similar branch of research that includes [18], which decomposes desired attitude control into MTAs and three independent torque axes.

For an attitude control system of three independent torques, it has been shown that almost global stability can be guaranteed by a PD feedback system for any choice of positive gains [27]. With the reduced system of an ACS consisting of only MTAs, stability is guaranteed within certain gain limits [14], but it remains that a PD control law is sufficient.

While other hybrid systems have been examined, the dynamics and optimal control laws for an ACS consisting of a VSCMG and MTAs have not been studied before. There are many possible approaches to defining optimality for such a system; one previously used by Damaren is to only use the impulsive thrusters when the MTAs are least capable of controlling the spacecraft [26]. While not necessarily optimal in terms of exertion and power consumption, it was reasonably used as a proxy for pointing performance. For the smaller spacecraft that a VSCMG/MTA hybrid is anticipated for, power consumption and exertion are considered to be more important factors; the former because power is more limited, and the latter because VSCMGs can saturate. When optimality conditions are properly defined (possibly as a weighting of multiple criteria), finding the optimal control laws then requires linearization of the model [11], leading to an LQR problem.

1.5 LQR Optimization

A general LQR problem is defined in Equations 1.3a and 1.3b, where T is the maximum convergence time, $\boldsymbol{x}$ is the state vector, $\boldsymbol{u}$ is the vector of inputs, and $\boldsymbol{Q}$ and $\boldsymbol{R}$ are symmetric cost matrices informed by the desired optimality conditions. It is a calculus of variations problem, where the goal is finding an optimal $\boldsymbol{u}(t)$ to minimize J. First, we define a value

function $V_{t_0}(\boldsymbol{z})$ as in Equation 1.3c, where $\boldsymbol{z} = \boldsymbol{x}(t_0)$. $V_{t_0}(\boldsymbol{z})$ gives the minimum cost left from $t_0 > 0$ to T. $V_{t_0}(\boldsymbol{z})$ can be put in the form of Equation 1.3d, as $\boldsymbol{u}$ can be defined in terms of $\boldsymbol{x}$. The optimal control laws are then found by computing the control matrix $\boldsymbol{K}$ in terms of the solution $\boldsymbol{X}$ to the continuous Riccati equation and (see Equations 1.3e, 1.3f). See [7] for everything in this paragraph.

$$\dot{\boldsymbol{x}} = \boldsymbol{A}\boldsymbol{x} + \boldsymbol{B}\boldsymbol{u} \tag{1.3a}$$

$$J = \int_0^T \left(\boldsymbol{x}(t)^T \boldsymbol{Q}\boldsymbol{x}(t) + \boldsymbol{u}(t)^T \boldsymbol{R}\boldsymbol{u}(t)\right) dt \tag{1.3b}$$

$$V_{t_0}(\boldsymbol{z}) = \min_{\boldsymbol{u}} \int_{t_0}^T \left(\boldsymbol{x}(t)^T \boldsymbol{Q}\boldsymbol{x}(t) + \boldsymbol{u}(t)^T \boldsymbol{R}\boldsymbol{u}(t)\right) dt \tag{1.3c}$$

$$V_{t_0}(\boldsymbol{z}) = \boldsymbol{z}^T \boldsymbol{X}\boldsymbol{z} \tag{1.3d}$$

$$\boldsymbol{A}^T\boldsymbol{X} + \boldsymbol{X}\boldsymbol{A} - \boldsymbol{X}\boldsymbol{B}\boldsymbol{R}^{-1}\boldsymbol{B}^T\boldsymbol{X} + \boldsymbol{Q} = \boldsymbol{0} \tag{1.3e}$$

$$\dot{\boldsymbol{x}} = \boldsymbol{A}\boldsymbol{x} + \boldsymbol{B}\boldsymbol{u} = \boldsymbol{A}\boldsymbol{x} - \boldsymbol{B}\boldsymbol{K}\boldsymbol{x} = \left(\boldsymbol{A} - \boldsymbol{B}\boldsymbol{R}^{-1}\boldsymbol{B}^T\boldsymbol{X}\right)\boldsymbol{x} \tag{1.3f}$$

This form of analysis however may prove simplistic if the desired mission requires large movements in the VSCMG. Linear approximations for the trigonometric functions in the torque equations (see Equation 2.9) only apply within a small range of the point of linearization, so unless the VSCMG gimbal motors moves relatively little, numerical analysis may be required to optimize this controller. This condition may only be met when the controller is used to hold a constant attitude, and even then for a short period of time, lest disturbance torques accumulate.

1.6 Magnetic Field Modelling

The position of the satellite is modelled with a circular Keplerian orbit (see Equations 1.4). Earth's magnetic field in the spacecraft body frame is modelled with the analytic approximation presented in Equations 1.5 taken from [24].

$$n = \sqrt{\frac{\mu}{R^3}} \tag{1.4a}$$

$$\boldsymbol{p}_i = R \begin{bmatrix} \cos(nt) \\ \sin(nt)\cos(\phi) \\ \sin(nt)\sin(\phi) \end{bmatrix} \tag{1.4b}$$

$$\boldsymbol{B}_i = \frac{B_0}{R^5}\begin{bmatrix} 3p_{i,x}p_{i,z} \\ 3p_{i,y}p_{i,z} \\ 2p_{i,z}^2 - p_{i,x}^2 - p_{i,y}^2 \end{bmatrix} \tag{1.5a}$$

$$\boldsymbol{B}_b = \boldsymbol{R}_b^i \boldsymbol{B}_i \tag{1.5b}$$

Where $\boldsymbol{R}_b^i$ is calculated from the orientation of the spacecraft. In a hypothetical spacecraft $\boldsymbol{B}_b$ would be found by an onboard magnetometer, and for reasons discussed later, it can be assumed that in the case of detumbling $\boldsymbol{B}_i$ is not known.

1.7 Disturbance Torques

As argued in [26], the dominant sources of disturbance torques are taken to be the spacecraft gravity gradient and residual magnetic field from the onboard electronics. These are modelled in Equation 1.6, where the terms are taken from Equations 1 and 1.1.

$$\vec{\tau}_{dist} = \vec{\tau}_{ggs} + \vec{\tau}_{resmag} = \vec{\mathcal{F}}_b \left(\frac{3\mu}{R^5} \boldsymbol{p}_b^{\times} \boldsymbol{I}_{sat} \boldsymbol{p}_b + \boldsymbol{m}_{dist}^{\times} \boldsymbol{B}_b \right) \tag{1.6}$$

The torque due to residual magnetic field may not be a steady torque. As systems are activated and deactivated at different points in the mission, the changing magnetic field will produce a jerky torque that the spacecraft will have to respond to immediately, perhaps even preemptively. This could lead to a further augmenting of the control system, or merely a test of disturbance response for a system unaware of residual fields.

The torque due to GGS is a much steadier disturbance than the residual field. Unless the moments of inertia are the same on all three principal axes or the 'heaviest' axis is lined up with the gravity gradient, a predictable and steady torque is applied. This poses an issue if the desired attitude results in a constant GGS torque, as the PD system will converge on a steady state attitude offset from the desired attitude. This is because at the steady state, the net torque is zero. However, there is a nonzero GGS torque. Since at steady state the D term will be zero, there must be a nonzero P term which produces a torque equal and opposite to the GGS torque. This implies a nonzero error at steady state.

The nonzero error can be resolved two ways: either the desired attitude sent to the controller is shifted so that the steady state converges on the real desired attitude, or an I term is added to the controller. This measures the time integral of the position error, also known as absement. If such a controller is used, then the integral of a nonzero error will accumulate until the difference is closed, requiring that the steady state error approaches zero.

Chapter 2

Dynamics of Proposed Spacecraft

2.1 Spacecraft Design

The spacecraft attitude control system being considered consists of one VSCMG and three independent, orthogonal MTAs. When rate limits are imposed, each MTA has a dipole moment limit of $m_{max} = \pm 12\ Am^2$.[15] The moment of inertia matrix is diagonal, which implies that the ACS is mounted such that its torques are exerted about the spacecraft's principal axes. The principal axis moments of inertia for the spacecraft are:

$$\boldsymbol{I}_{sat} = \begin{bmatrix} 21 & 0 & 0 \\ 0 & 25 & 0 \\ 0 & 0 & 27 \end{bmatrix} kgm^2 \tag{2.1}$$

The moment of inertia for the gryoscope in the VSCMG is $I_g = 0.001 kgm^2$ about the spinning axis and assumed to be negligible about the other two. It starts at an initial angular speed of $\Omega_g = 200\pi\ rad/s = 6000 RPM$. When rate limits are imposed, the gimbal rates are limited to $\dot{\gamma}_{max} = \pm 5\ deg/s = \pm\pi/36\ rad/s$ and the gyro acceleration is limited to $\dot{\Omega}_{g,max} = \pm 10\ rad/s^2$. These VSCMG characteristics were taken from the design proposed in [19] for small spacecraft.

The residual magnetic dipole is:

$$\boldsymbol{m}_{res} = \begin{bmatrix} 0.001 \\ 0.001 \\ 0.001 \end{bmatrix} Am^2 \tag{2.2}$$

The spacecraft is orbiting the Earth at an altitude of $400km$ and an inclination of $40deg$ above the equator.

2.2 Dynamics Equations

2.2.1 VSCMG Dynamics

The torque applied by a VSCMG was calculated assuming:

1. Negligible moments of inertia for the gimbal carriage.

2. Angular rates of the gimbal axes $\dot{\gamma}_o$ and $\dot{\gamma}_i$ are much smaller than Ω_g.

To derive $\vec{\tau}_{vscmg}$, we start with the angular momentum in the gyro frame:

$$\boldsymbol{L}_g = \begin{bmatrix} 0 & 0 & I_g\Omega_g \end{bmatrix}^T \tag{2.3}$$

First the single-gimbal case is considered. This is to demonstrate the same derivation process as is used in the double-gimbal case, even though it is not part of the assumed spacecraft design. To bring the angular momentum into the body frame, we require rotation matrices from the gyro to the gimbal carriage ($\boldsymbol{R}_c^g$) and from the gimbal carriage to the body ($\boldsymbol{R}_b^c$). For each reference frame, the z axis is parallel to the local revolute joint and the x axis is normal to the plane containing the previous and next revolute joints. The rotation matrices are:

$$\boldsymbol{R}_c^g = \begin{bmatrix} 0 & -1 & 0 \\ 0 & 0 & 1 \\ -1 & 0 & 0 \end{bmatrix}, \boldsymbol{R}_b^c = \begin{bmatrix} -\sin(\gamma) & -\cos(\gamma) & 0 \\ 0 & 0 & 1 \\ -\cos(\gamma) & \sin(\gamma) & 0 \end{bmatrix} \tag{2.4}$$

The angular momentum in the body frame is therefore:

$$\boldsymbol{L}_{sgcmg,b} = \boldsymbol{R}_b^c\boldsymbol{R}_c^g\boldsymbol{L}_g = \begin{bmatrix} -I_g\cos(\gamma)\Omega_g \\ 0 \\ I_g\sin(\gamma)\Omega_g \end{bmatrix} \tag{2.5}$$

Taking the derivative to get torque, we find that it is now a linear function of the gimbal rate and gyro acceleration, where the matrix operator $\boldsymbol{H}$ is a function of the VSCMG's state $\boldsymbol{s}$:

$$\begin{aligned} \vec{\tau}_{sgcmg} &= \vec{\mathcal{F}}_b I_g \begin{bmatrix} \sin(\gamma)\Omega_g & -\cos(\gamma) \\ 0 & 0 \\ \cos(\gamma)\Omega_g & \sin(\gamma) \end{bmatrix} \begin{bmatrix} \dot{\gamma} \\ \dot{\Omega}_g \end{bmatrix} \\ &= \vec{\mathcal{F}}_b \boldsymbol{H}(\boldsymbol{s})\dot{\boldsymbol{s}} \end{aligned} \tag{2.6}$$

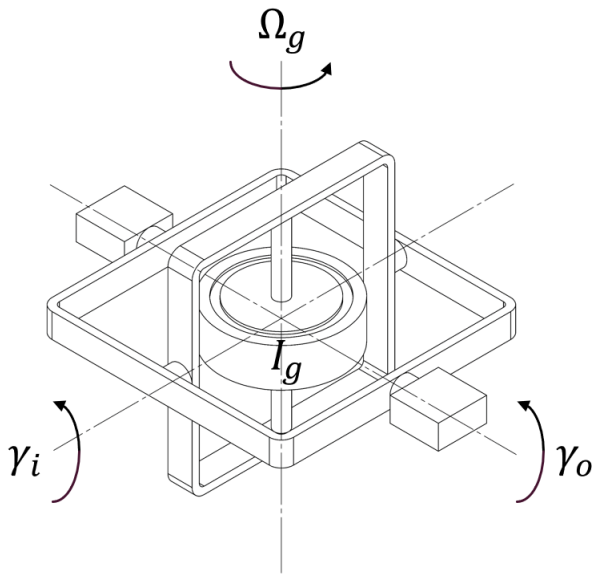

Figure 2.1: Double-Gimbal VSCMG with Zero Gimbal Angles

For the double-gimbal case as in Figure 2.1, we require three rotation matrices: from the gyro to the inner gimbal ($\boldsymbol{R}_i^g$), from the inner gimbal to the outer gimbal ($\boldsymbol{R}_o^i$), and from the outer gimbal to the body ($\boldsymbol{R}_b^o$). For each reference frame, again the z axis is parallel to the local revolute joint and the x axis is normal to the plane containing the previous and next revolute joints. The rotation matrices are:

$$\boldsymbol{R}_i^g = \begin{bmatrix} 0 & -1 & 0 \\ 0 & 0 & 1 \\ -1 & 0 & 0 \end{bmatrix}, \boldsymbol{R}_o^i = \begin{bmatrix} -\sin(\gamma_i) & -\cos(\gamma_i) & 0 \\ 0 & 0 & 1 \\ -\cos(\gamma_i) & \sin(\gamma_i) & 0 \end{bmatrix}, \boldsymbol{R}_b^o = \begin{bmatrix} -\sin(\gamma_o) & -\cos(\gamma_o) & 0 \\ 0 & 0 & 1 \\ -\cos(\gamma_o) & \sin(\gamma_o) & 0 \end{bmatrix} \tag{2.7}$$

The angular momentum in the body frame is therefore:

$$\boldsymbol{L}_{dgcmg,b} = \boldsymbol{R}_b^o \boldsymbol{R}_o^i \boldsymbol{R}_i^g \boldsymbol{L}_g = \begin{bmatrix} I_g \sin(\gamma_o)\cos(\gamma_i)\Omega_g \\ I_g \sin(\gamma_i)\Omega_g \\ I_g \cos(\gamma_o)\cos(\gamma_i)\Omega_g \end{bmatrix} \tag{2.8}$$

Taking the derivative to get torque, we find again that it is now a linear function of the

gimbal rates and gyro acceleration. Here, $\boldsymbol{G}$ represents the matrix function of state $\boldsymbol{c}$:

$$\begin{aligned}\vec{\tau}_{dgcmg} &= \vec{\mathcal{F}}_b I_g \begin{bmatrix} \cos(\gamma_o)\cos(\gamma_i)\Omega_g & -\sin(\gamma_o)\sin(\gamma_i)\Omega_g & \sin(\gamma_o)\cos(\gamma_i) \\ 0 & \cos(\gamma_i)\Omega_g & \sin(\gamma_i) \\ -\sin(\gamma_o)\cos(\gamma_i)\Omega_g & -\cos(\gamma_o)\sin(\gamma_i)\Omega_g & \cos(\gamma_o)\cos(\gamma_i) \end{bmatrix} \begin{bmatrix} \dot{\gamma}_o \\ \dot{\gamma}_i \\ \dot{\Omega}_g \end{bmatrix} \\ &= \vec{\mathcal{F}}_b \boldsymbol{G}(\boldsymbol{c})\dot{\boldsymbol{c}}\end{aligned} \tag{2.9}$$

The G matrix has singularities at $\Omega_g = 0$ and at $\gamma_i = \pm\frac{\pi}{2}$, which means that in those conditions the VSCMG has fewer than all three degrees of freedom. Because the proposed spacecraft design includes a double-gimbal VSCMG, references to $\vec{\tau}_{vscmg}$ elsewhere in the document can be taken to refer to $\vec{\tau}_{dgcmg}$.

2.2.2 Total Dynamics Equation

For rigid body dynamics the Euler equation for rigid body dynamics is used, with the torques due to the VSCMG (Equation 2.9), MTAs (Equation 1), gravity gradient (Equation 1.1), and residual magnetic field on the RHS, resulting in Equation 2.10. The equation is then rearranged into state space form (see Equation 2.11).

$$\begin{aligned}\vec{\mathcal{F}}_b \left(\boldsymbol{I}_{sat}\dot{\boldsymbol{\omega}} + \boldsymbol{\omega}^{\times} \left(\boldsymbol{I}_{sat}\boldsymbol{\omega} + \boldsymbol{L}_{dgcmg,b} \right) \right) &= \sum_i \vec{\tau}_i = \vec{\tau}_{vscmg} + \vec{\tau}_{mta} + \vec{\tau}_{ggs} + \vec{\tau}_{resmag} \\ &= \vec{\mathcal{F}}_b \left(\boldsymbol{G}\dot{\boldsymbol{c}} + \boldsymbol{m}^{\times}\boldsymbol{B}_b + \frac{3\mu}{R^5}\boldsymbol{p}_b^{\times}\boldsymbol{I}_{sat}\boldsymbol{p}_b + \boldsymbol{m}_{res}^{\times}\boldsymbol{B}_b \right)\end{aligned} \tag{2.10}$$

$$\dot{\boldsymbol{\omega}} = \boldsymbol{I}_{sat}^{-1} \left[\boldsymbol{G}\dot{\boldsymbol{c}} + \boldsymbol{m}^{\times}\boldsymbol{B}_b + \frac{3\mu}{R^5}\boldsymbol{p}_b^{\times}\boldsymbol{I}_{sat}\boldsymbol{p}_b + \boldsymbol{m}_{res}^{\times}\boldsymbol{B}_b - \boldsymbol{\omega}^{\times} \left(\boldsymbol{I}_{sat}\boldsymbol{\omega} + \boldsymbol{L}_{dgcmg,b} \right) \right] \tag{2.11}$$

And now we require control laws to determine the inputs $\dot{\boldsymbol{c}}$ and $\boldsymbol{m}$. The former not only determines the input, but forms a state-space equation of its own for the VSCMG state $\boldsymbol{c}$, which is needed to calculate $\boldsymbol{G}$.

In the following chapters, nonlinear and LQR control laws will be proposed and evaluated for two scenarios: detumbling a spacecraft from some initial angular velocity, and holding a spacecraft at a desired angular position.

Chapter 3

Nonlinear Control

3.1 Detumbling Control Feedback

Assuming the spacecraft has nonzero initial angular velocity (e.g. because it was just ejected from the rocket that carried it into orbit), this controller must bring the angular velocity to zero. For detumbling, the final orientation is not important as long as it is constant.

3.1.1 Proposed Control Laws

The control feedback laws for $\boldsymbol{m}$ and $\dot{\boldsymbol{c}}$ therefore follow the angular rates of the spacecraft and Earth's magnetic field, as shown in Equations 3.1 and 3.2.

$$\boldsymbol{m} = -K_m \dot{\boldsymbol{B}}_b \tag{3.1}$$

$$\dot{\boldsymbol{c}} = -\boldsymbol{K}_c \boldsymbol{G}^T \boldsymbol{\omega} \tag{3.2}$$

$$\boldsymbol{K_d} = \begin{bmatrix} K_{c,g} & 0 & 0 \\ 0 & K_{c,g} & 0 \\ 0 & 0 & K_{c,w} \end{bmatrix} \tag{3.3}$$

Where K_m is a scalar gain and $\boldsymbol{K}_c$ is a diagonal matrix of gains. $\boldsymbol{K}_c$ takes the form shown in Equation 3.3, where $K_{c,g}$ is the gain for the gimbal carriages and $K_{c,w}$ is the gain for the flywheel. From the definition for $\boldsymbol{G}(\boldsymbol{c})$ in Equation 2.9, the torque applied by an equivalent change in $\dot{\gamma}_o$ or $\dot{\gamma}_i$ and $\dot{\Omega}_g$ differs by a factor of Ω_g, therefore to equalize the torque on all three axes, $K_{c,w} = \Omega_g K_{c,g}$. References to $K_{c,x}$ elsewhere in the document where x is a different or no subscript can be taken to refer to $K_{c,g}$.

The control law for $\boldsymbol{m}$ in terms of $\dot{\boldsymbol{B}}_b$ will attempt to follow the magnetic field line rather than the absolute angular position of the spacecraft. This can be useful if the spacecraft

is supposed to keep a certain side facing the ground, but otherwise it would be preferable to have a control law in terms of $\boldsymbol{\omega}$. This can be recovered through an approximation. The derivative in the body frame would normally be calculated through Equation 3.4. But with the assumption that our spacecraft's angular rates are much faster than the change in magnetic field in the inertial frame due to the spacecraft's orbit around the Earth, we assume that $\dot{\boldsymbol{B}}_i \approx 0$, leading to Equation 3.5.

$$\dot{\boldsymbol{B}}_i = \dot{\boldsymbol{B}}_b + \boldsymbol{\omega}^\times \boldsymbol{B}_b \tag{3.4}$$

$$\dot{\boldsymbol{B}}_b \approx -\boldsymbol{\omega}^\times \boldsymbol{B}_b = \boldsymbol{B}_b^\times \boldsymbol{\omega} \tag{3.5}$$

And this all can be incorporated back into Equation 2.11, producing Equation 3.6.

$$\dot{\boldsymbol{\omega}} = \boldsymbol{I}_{sat}^{-1}\left[-\boldsymbol{G}\boldsymbol{K}_c\boldsymbol{G}^T\boldsymbol{\omega} - K_m\boldsymbol{B}_b^\times\boldsymbol{B}_b^\times\boldsymbol{\omega} + \frac{3\mu}{R^5}\boldsymbol{p}_b^\times\boldsymbol{I}_{sat}\boldsymbol{p}_b + \boldsymbol{m}_{res}^\times\boldsymbol{B}_b - \boldsymbol{\omega}^\times\left(\boldsymbol{I}_{sat}\boldsymbol{\omega} + \boldsymbol{L}_{cmg}\right)\right] \tag{3.6}$$

To compute $\boldsymbol{G}$, the equation for $\dot{\boldsymbol{c}}$ (Equation 3.2) must be solved in parallel to Equation 3.6.

3.1.2 Lyapunov Stability of Detumbling Controller

Stability is determined by the rate of change of kinetic energy (see Equation 3.7), which must be ≤ 0. The $\dot{\boldsymbol{\omega}}$ term can be filled in using Equation 3.6, producing Equation 3.8. The disturbance torques are neglected here as they are much smaller in magnitude than the active torques. We first observe that the last term must be zero, leaving the two control terms. $\boldsymbol{B}_b^\times\boldsymbol{B}_b^\times$ as the product of two cross product matrices is negative semidefinite, therefore for all $K_m < 0$, $-K_m\boldsymbol{\omega}^T\boldsymbol{B}_b^\times\boldsymbol{B}_b^\times\boldsymbol{\omega} \leq 0$. If the diagonal elements of $\boldsymbol{K}_c$ are all > 0, then because $\boldsymbol{G}\boldsymbol{G}^T$ is positive semidefinite, $\boldsymbol{G}\boldsymbol{K}_c\boldsymbol{G}^T$ is also positive semidefinite. Therefore $-\boldsymbol{\omega}^T\boldsymbol{G}\boldsymbol{K}_c\boldsymbol{G}^T\boldsymbol{\omega} \leq 0$. Because both terms are less than or equal to 0, it follows that $\dot{E}_k \leq 0$, meaning the system is stable.

$$E_k = \frac{1}{2}\boldsymbol{\omega}^T\boldsymbol{I}_{sat}\boldsymbol{\omega} \Rightarrow \dot{E}_k = \boldsymbol{\omega}^T\boldsymbol{I}_{sat}\dot{\boldsymbol{\omega}} \tag{3.7}$$

$$\begin{aligned}\dot{E}_k &= \boldsymbol{\omega}^T\left[-\boldsymbol{G}\boldsymbol{K}_c\boldsymbol{G}^T\boldsymbol{\omega} - K_m\boldsymbol{B}_b^\times\boldsymbol{B}_b^\times\boldsymbol{\omega} - \boldsymbol{\omega}^\times\left(\boldsymbol{I}_{sat}\boldsymbol{\omega} + \boldsymbol{L}_{cmg}\right)\right] \\ &= -\boldsymbol{\omega}^T\boldsymbol{G}\boldsymbol{K}_c\boldsymbol{G}^T\boldsymbol{\omega} - K_m\boldsymbol{\omega}^T\boldsymbol{B}_b^\times\boldsymbol{B}_b^\times\boldsymbol{\omega} - \boldsymbol{\omega}^T\boldsymbol{\omega}^\times\left(\boldsymbol{I}_{sat}\boldsymbol{\omega} + \boldsymbol{L}_{cmg}\right) \\ &= -\boldsymbol{\omega}^T\boldsymbol{G}\boldsymbol{K}_c\boldsymbol{G}^T\boldsymbol{\omega} - K_m\boldsymbol{\omega}^T\boldsymbol{B}_b^\times\boldsymbol{B}_b^\times\boldsymbol{\omega}\end{aligned} \tag{3.8}$$

As will be seen in simulations in Section 3.3, when the disturbance torques are comparable in magnitude to the active torques, kinetic energy no longer tends monotonically to zero.

3.2 Extension to PD Controller

The controller discussed so far was just the detumbling controller, as the control inputs are proportional to the angular velocity $\boldsymbol{\omega}$. If there is no angular velocity, there is no control input. Because it is proportional to the derivative of angular position, it is a D controller. To not just detumble the spacecraft but to also maintain a given position, the controller must also produce corrective input when the position error is nonzero. Position is represented here using the vector component $\boldsymbol{\epsilon}$ of the unit quaternion $\boldsymbol{q} = \begin{bmatrix} \eta & \boldsymbol{\epsilon} \end{bmatrix}$. The unit quaternion was chosen to represent orientation because it lacks the issue of singularities (gimbal-lock) associated with Euler angles. The propotional-derivative (PD) controller makes use of the same control laws for both terms as per Equation 3.9, with new control gains $K_{m,p}$ and $\boldsymbol{K}_{c,p}$ for the P terms. The controller will attempt to bring the spacecraft to the state where $\boldsymbol{\omega} = 0$, $\boldsymbol{\epsilon} = 0$, and $\eta = 1$ (because for a unit quaternion, $|\boldsymbol{q}| = 1$).

$$\boldsymbol{m} = -K_{m,d}\boldsymbol{B}_b^{\times}\boldsymbol{\omega} - K_{m,p}\boldsymbol{B}_b^{\times}\boldsymbol{\epsilon} \tag{3.9a}$$

$$\dot{\boldsymbol{c}} = -\boldsymbol{K}_{c,d}\boldsymbol{G}^T\boldsymbol{\omega} - \boldsymbol{K}_{c,p}\boldsymbol{G}^T\boldsymbol{\epsilon} \tag{3.9b}$$

While $\boldsymbol{\epsilon}$ is usually written with a 2 coefficient to relate it to the magnitude of the rotation angle, this has been absorbed into the gains $K_{m,p}$ and $\boldsymbol{K}_{c,p}$ for brevity.

3.3 Steady-State Simulations

This scenario starts the spacecraft in the desired state. All that is required of the controller is to respond to the disturbance torques due to GGS and residual magnetic field. This is only doable with a PD controller, so the control laws in Equation 3.9 are used.

3.3.1 Error Minimization with Gains Tuning

To reduce the degrees of freedom involved with tuning the nonlinear controller from 4 to 2, the D gains were chosen arbitrarily to be the independent variables, and the Matlab built-in optimizer fmincon would be utilized to find an optimal ratio of the D and P gains to minimize the mean square error in $\boldsymbol{\epsilon}$ over a half orbital period. This mean square error is used to evaluate the chosen gains in Figure 3.1, and the corresponding optimized gain ratios are given in Figure 3.2. The range of D gains tested were $K_{m,d} \in [10^6, 10^{10}]$ and $K_{c,d} \in [10^{-2}, 10^1]$. For these simulations, no rate limits have been imposed on the controllers. Note that the two spikes that appear in Figure 3.1 do not represent the genuine behaviour of the error plot; those are merely where fmincon failed to properly converge.

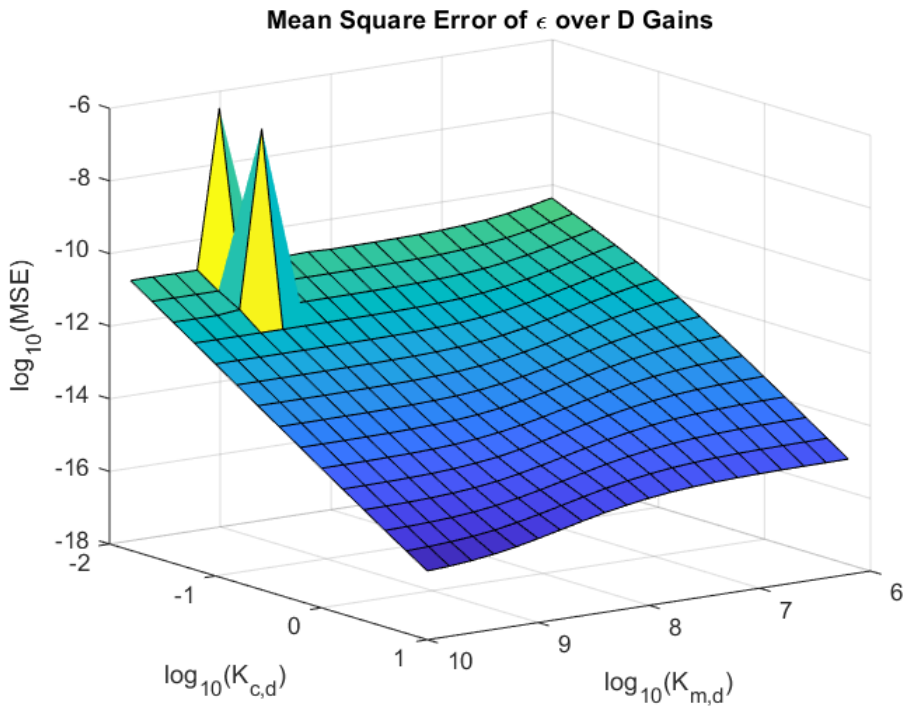

Figure 3.1: Mean Square Error over VSCMG and MTA D gains

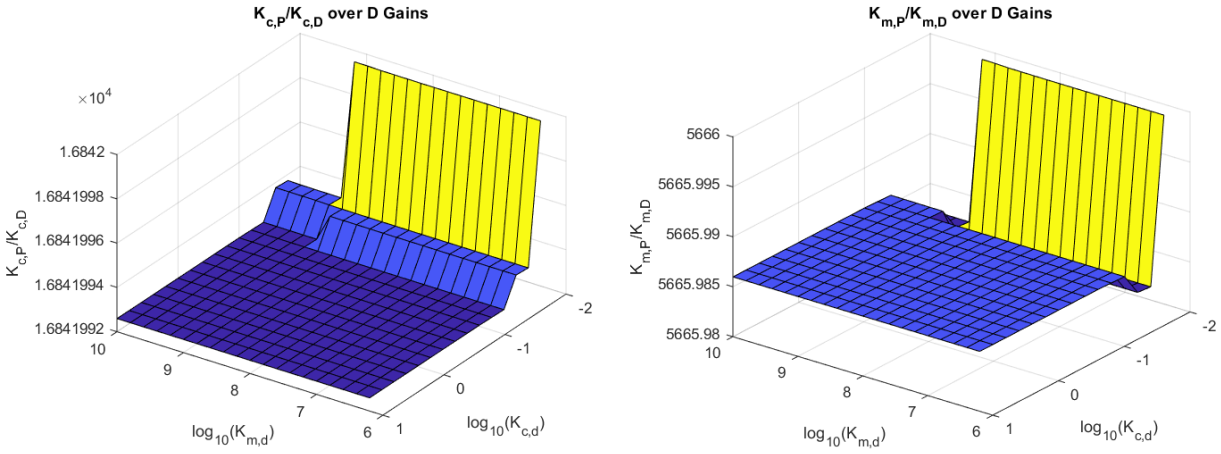

(a) VSCMG P/D Gain Ratio over D Gains (b) MTA P/D Gain Ratio over D Gains

Figure 3.2: P/D Gain Ratios Over $K_{m,d}$ and $K_{c,d}$

The gain ratios stay close to constant over the examined range of gains, with $K_{c,p} \approx 5666K_{c,d}$ and $K_{m,p} \approx 16842K_{m,d}$, suggesting these are at least local optima. What we see in Figure 3.1 is a strong decrease in mean square error with increase in the VSCMG gain, but the MTA gain is only effective within a region. Before and after this region, the error is close to constant with respect to the MTA gain.

For $\log_{10}(K_{c,d}) = -0.2$ the lower bound $\log_{10}(K_{m,d,lb}) \approx 6.2$ and the upper bound $\log_{10}(K_{m,d,ub}) \approx 8.8$. For $\log_{10}(K_{c,d}) = 0.8$ the lower bound $\log_{10}(K_{m,d,lb}) \approx 7.2$ and the upper bound $\log_{10}(K_{m,d,ub}) \approx 9.8$. The approximate correlations are $\log_{10}(K_{m,d,lb}) = \log_{10}(K_{c,d}) - 6.4$ and $\log_{10}(K_{m,d,ub}) = \log_{10}(K_{c,d}) - 9$. Between these two regions, the MTA gain decreases the error by a consistent factor of approximately $10^{1.2}$.

3.3.2 Simulation of Key Cases

Physically, the lower bound corresponds to when the magnitude of MTA torque is large enough to be significant against the VSCMG torque, and the upper bound corresponds to when the torque exerted by the MTAs matches that of the VSCMG in magnitude. Figure 3.3 is taken with $K_{c,d} = -0.4$ and the $K_{m,d}$ lower bound of $K_{m,d} = 6$, and we can see that the torques from the VSCMG reach a magnitude of $10^{-5}\ Nm$, an order of magnitude higher than the MTA torques of under $10^{-6}\ Nm$. Figure 3.4 is taken at the upper bound of $K_{m,d} = 8.6$. The MTAs and VSCMG now have very close torque magnitudes of approximately $5 \times 10^{-5}\ Nm$. If $K_{c,d}$ is reduced to -1.4, $K_{m,d} = 8.6$ is now well past the effective region's upper bound of 7.6, but as Figure 3.5 shows, the magnitudes of torque from both the VSCMG and MTA remain stubbornly similar. This is not due to the performance limits being reached; the MTA dipole moments are several orders of magnitude below their maximum. This is because the VSCMG is necessary to fill in the lost degree of freedom inherent to MTA systems, so beyond the point where similar torques are achieved, no further increase to the difference between gains will diminish the VSCMG in favour of the MTA.

A simulation is provided where the VSCMG gains are zeroed and the MTA gains are kept exactly the same as in Figure 3.4 to illustrate the difference the VSCMG makes. While angle error is on the order of $10^{-8}\ rad$ in Figure 3.4, it increases to $0.2\ rad$ when the VSCMG is disabled in the simulation shown in Figure 3.6. Here we see that when it comes to steady state angular position, the hybrid VSCMG MTA ACS is a huge improvement over a pure MTA system.

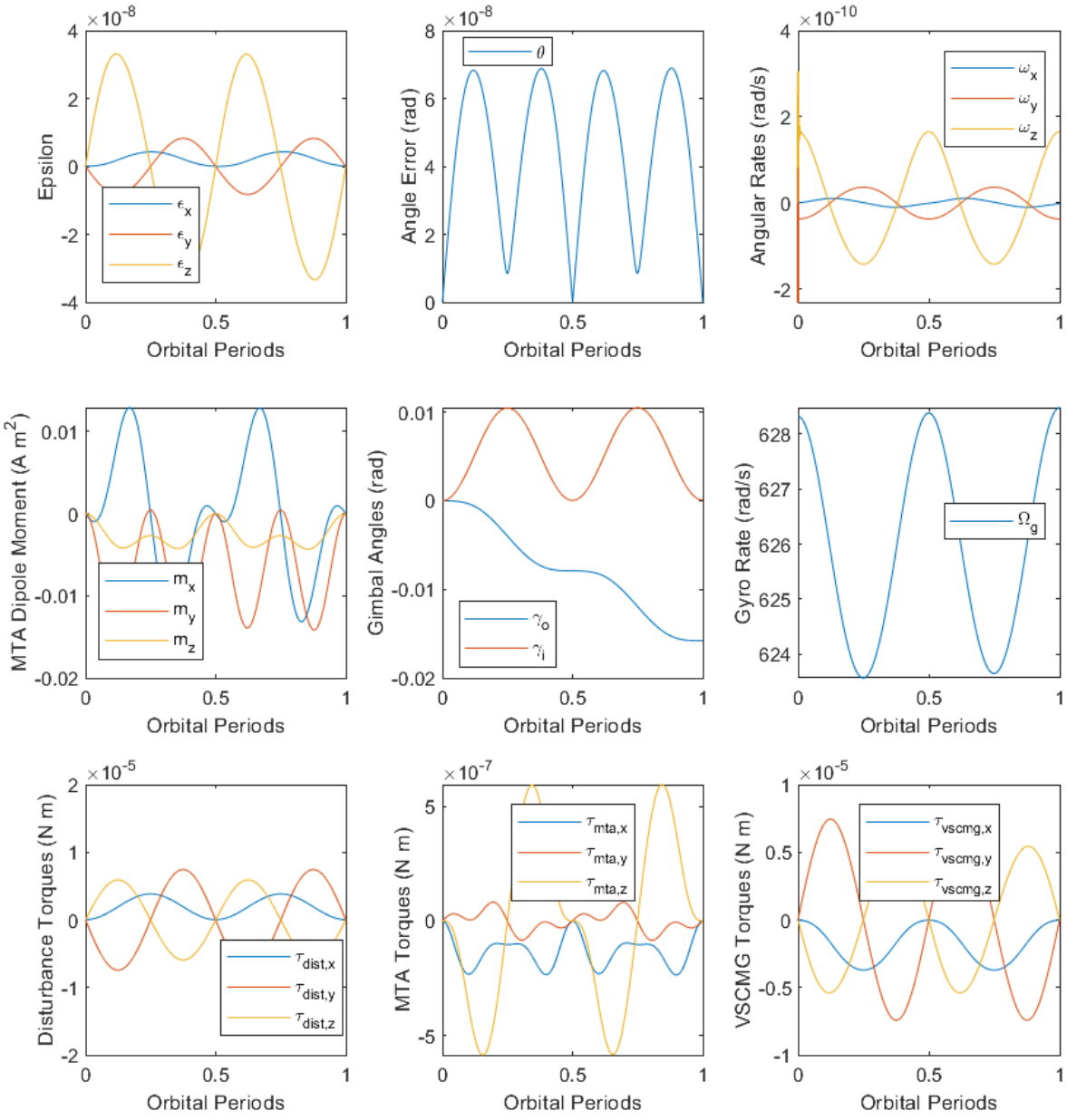

Figure 3.3: Simulation of Steady-State where $K_{c,d} = 10^{-0.4}$, $K_{m,d} = 10^{6}$

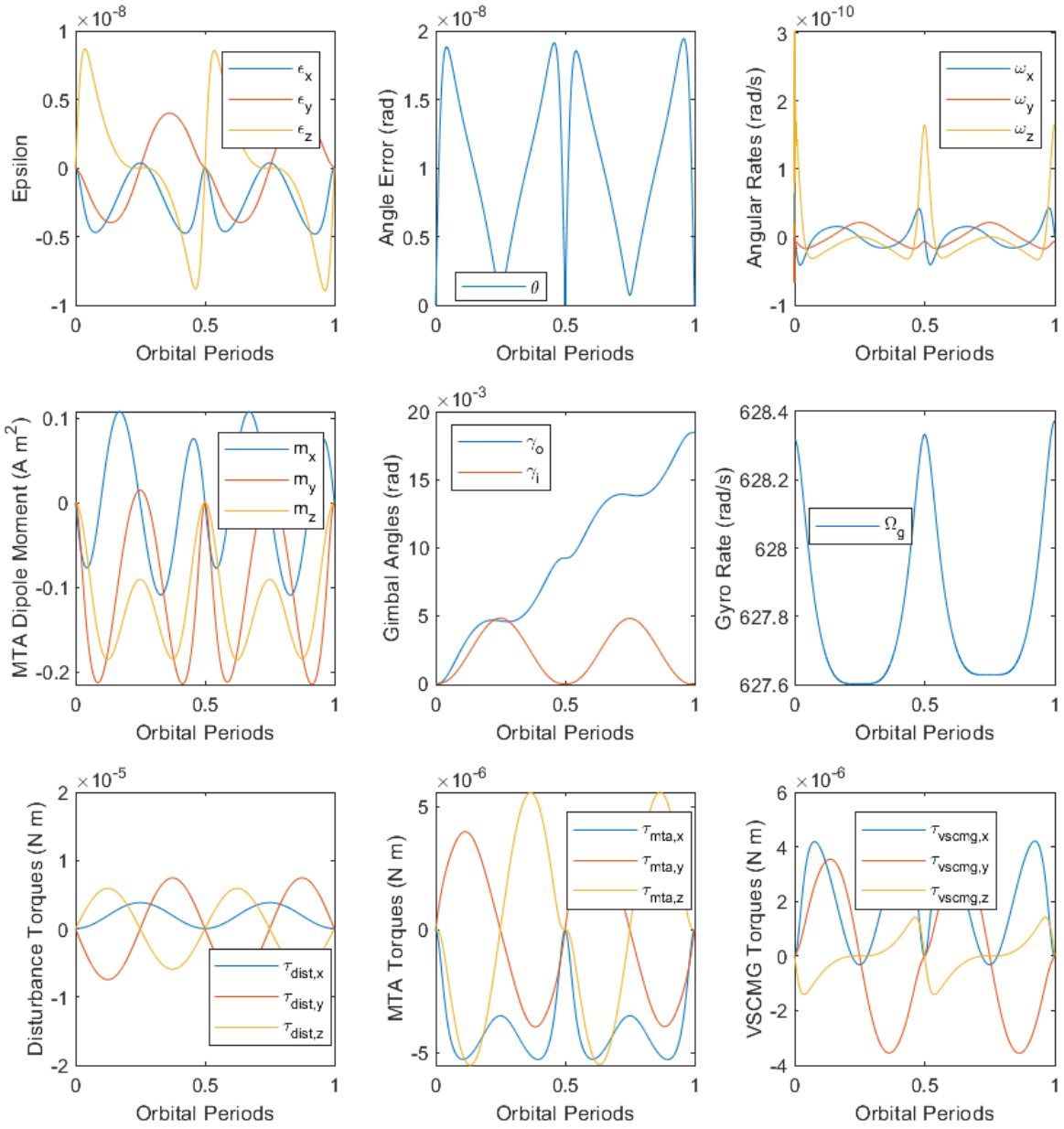

Figure 3.4: Simulation of Steady-State where $K_{c,d} = 10^{-0.4}$, $K_{m,d} = 10^{8.6}$

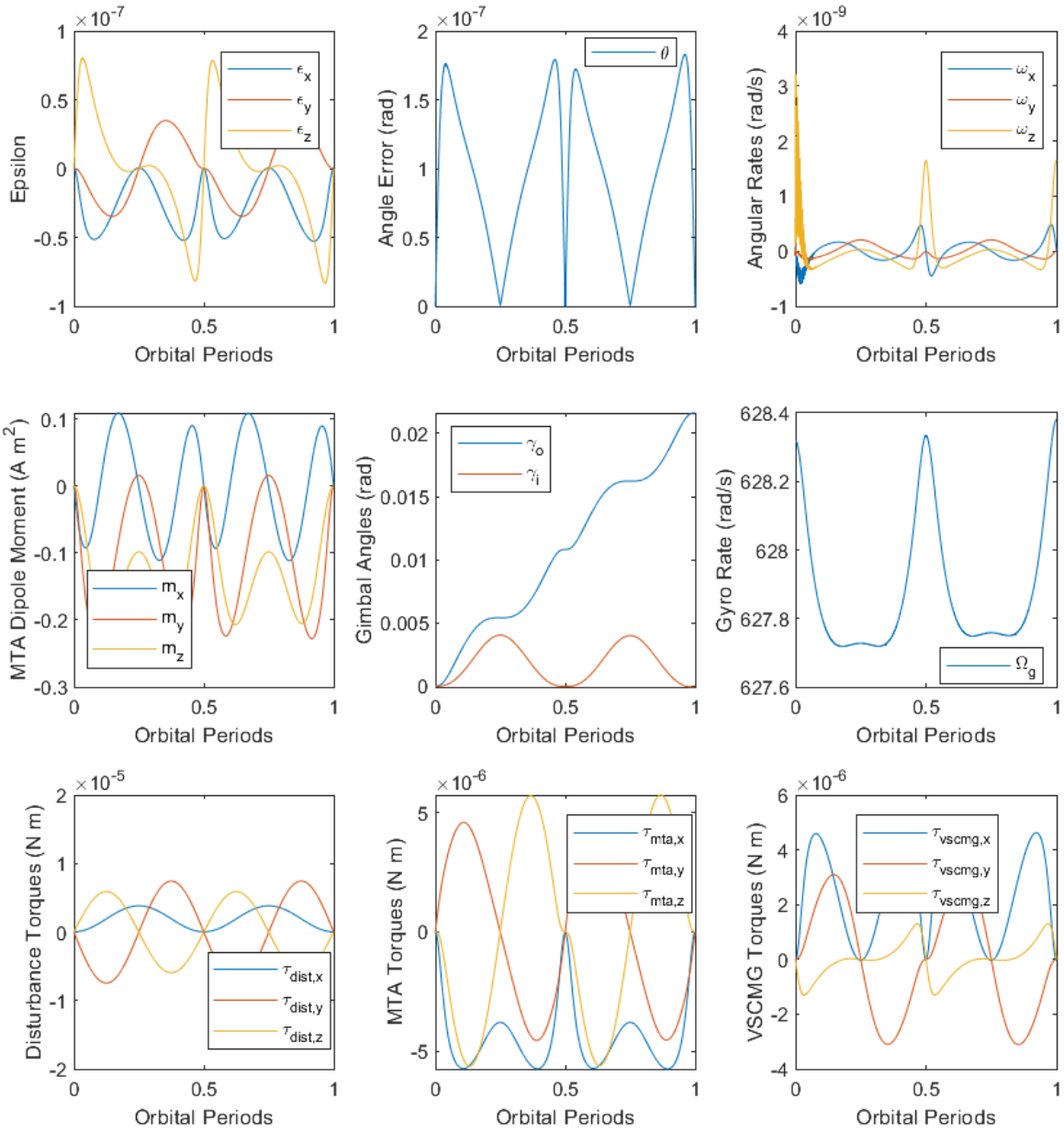

Figure 3.5: Simulation of Steady-State where $K_{c,d} = 10^{-1.4}$, $K_{m,d} = 10^{8.6}$

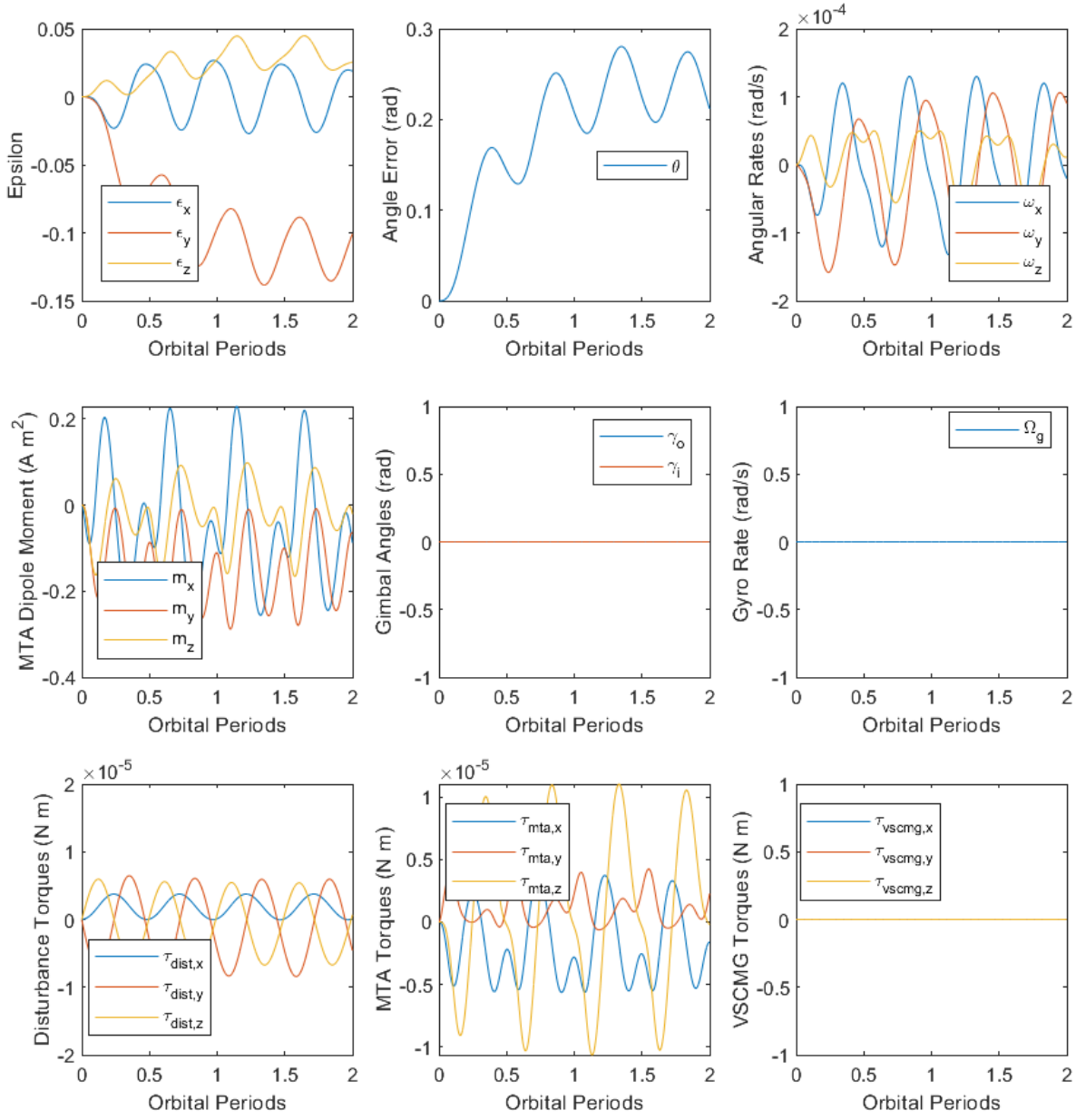

Figure 3.6: Simulation of Steady-State where $K_{c,d} = 0$, $K_{m,d} = 10^{8.6}$

3.4 Detumbling Simulations

This scenario starts the spacecraft with an angular velocity and requires it to slow down and stop. This can be done with either a D or PD controller. If the former, then the spacecraft will stop in an arbitrary position. If the latter, the spacecraft will attempt to return to a "home" position.

3.4.1 D Controller

The simulations in this section make use of the control laws in Equation 3.6. As implied by the Lyapunov stability proof in Section 3.1.2, there is a monotonic decrease in convergence time with increased D gains. There are physical upper bounds however; the controllers cannot actuate the MTAs and VSCMG beyond their performance limits. These rather unsophisticated performance predictions are borne out by the simulations in Figures 3.7 to 3.9.

The initial angular rate chosen was $\boldsymbol{\omega}_0 = \begin{bmatrix} 10 & 0 & 0 \end{bmatrix}^T deg/s = \begin{bmatrix} \pi/18 & 0 & 0 \end{bmatrix}^T rad/s$.

The simulations in Figures 3.7, 3.8, and 3.9 are conducted using the VSCMG/MTA D gain ratio for equal torque found in Section 3.3.1. They are each offset by one order of magnitude from each other. We see in Figure 3.7 that convergence time is fairly long at approximately 1 orbital period and while the actuators do hit their performance limits, these periods are fairly early and short. With higher gains, the convergence time shortens and the actuators spend more time operating at their performance limits. This is shown in Figure 3.9, where the gyroscope acceleration and MTAs in particular spend large portions of the convergence time operating at their limits, and the convergence time shortens to roughly 7% of an orbital period.

The trend is also apparent that with higher gains, the VSCMG torques overwhelm the MTA torques. This is because the MTAs hit their performance limits with fairly low gains, unlike the VSCMG. When both actuator types are inside their performance limits, they do produce torques of similar magnitude.

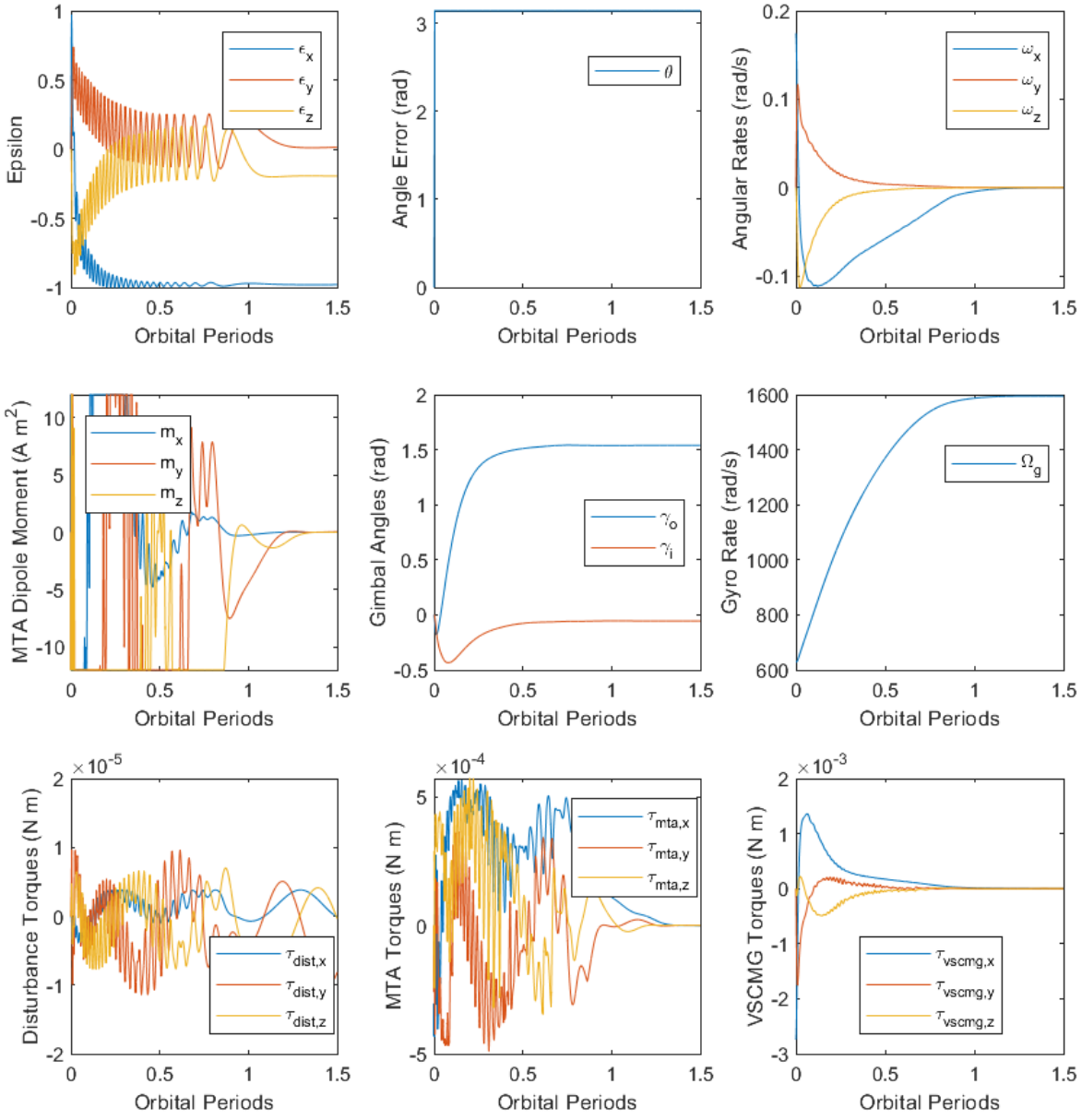

Figure 3.7: Simulation of D-Controller Detumbling where $K_{c,d} = 10^{-1.4}$, $K_{m,d} = 10^{7.6}$

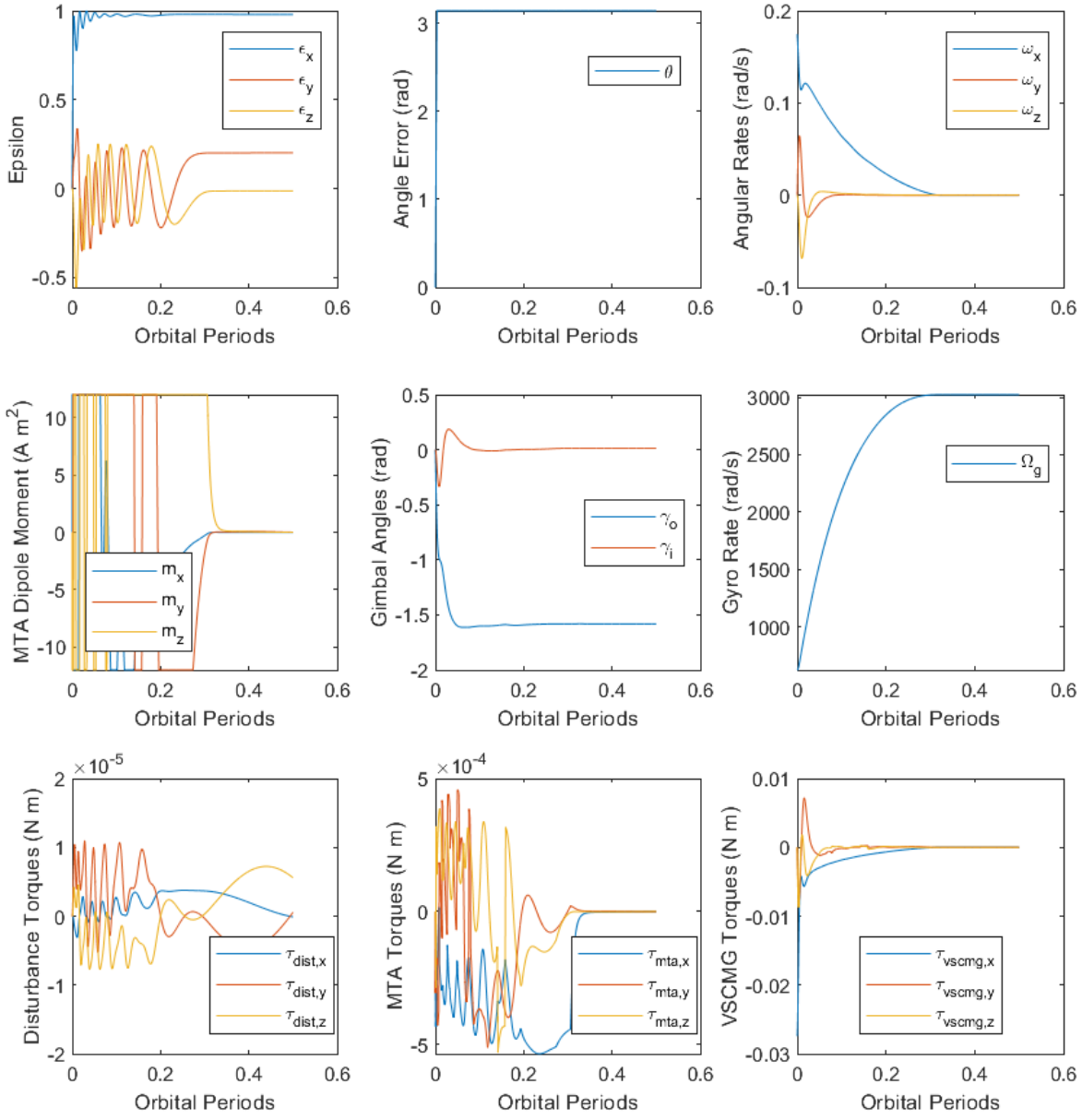

Figure 3.8: Simulation of D-Controller Detumbling where $K_{c,d} = 10^{-0.4}$, $K_{m,d} = 10^{8.6}$

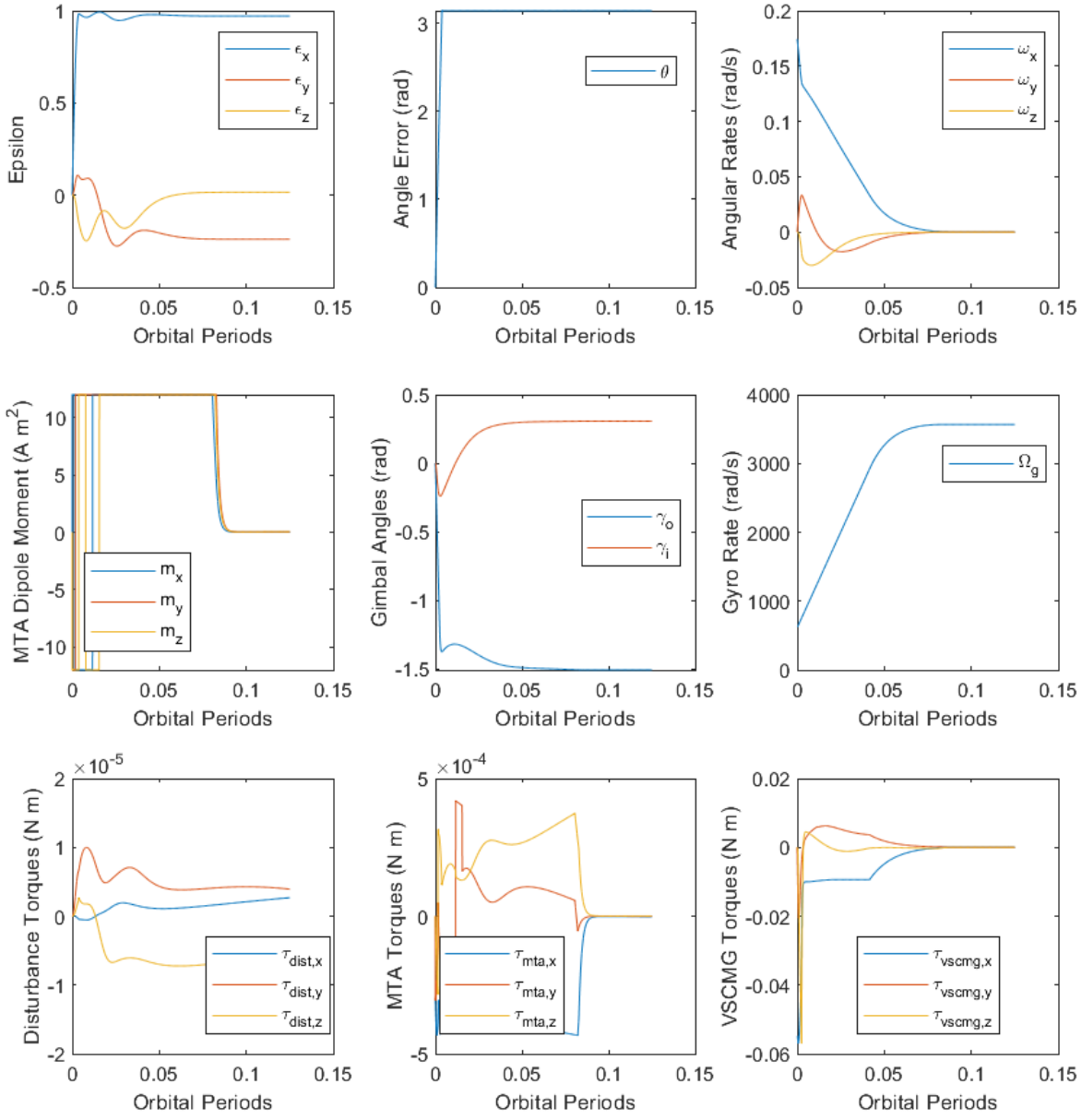

Figure 3.9: Simulation of D-Controller Detumbling where $K_{c,d} = 10^{0.6}$, $K_{m,d} = 10^{9.6}$

3.4.2 PD Controller

The simulations in this section make use of the control laws in Equation 3.9. The use of a PD controller leads to different convergence criteria than just a D controller: the spacecraft is considered to be "converged" when both the angular position ϵ and the angular velocity ω are sufficiently small.

To focus on the controllers returning to position rather than the spacecraft deceleration, the initial angular velocity is reduced to $\boldsymbol{\omega}_0 = \begin{bmatrix} 3 & 0 & 0 \end{bmatrix}^T deg/s = \begin{bmatrix} \pi/60 & 0 & 0 \end{bmatrix}^T rad/s$.

A similar method to Section 3.3 was used to choose gains for simulation. $K_{c,d}$ and $K_{m,d}$ were independently varied and Matlab's fmincon optimizer was used to find optimal $K_{c,p}$ and $K_{m,p}$ as ratios of their corresponding D gain. The objective it was optimized against however was not MSE error, as that is not as meaningful for this scenario as it is for steady-state. The objective here is convergence time, i.e. the time from the simulation start to when the absolute values of the terms in $\boldsymbol{\epsilon}$, $\boldsymbol{\omega}$, $\dot{\boldsymbol{c}}$, and $\boldsymbol{m}$ are all less than a tolerance value, chosen to be 10^{-3}.

Three sets of gains were tested. All three had a 9 order of magnitude separation between $K_{c,d}$ and $K_{m,d}$ as in the last section. In Figure 3.10, $K_{c,d} = 10^0$ and the controller converges in about a quarter orbital period. The MTA is at its dipole limit for most of the simulation, leading to the VSCMG overwhelming it in applied torque. As expected higher gains lead to faster convergence; Figure 3.11 has a convergence time of a little over 5% of an orbital period. Here however, the gyro is clearly at its acceleration limit for most of the simulation. With both actuators operating close to their limits, it is no surprise that in Figure 3.12, despite the $K_{c,d}$ being increased by another order of magnitude, it barely converges any faster than the last simulation.

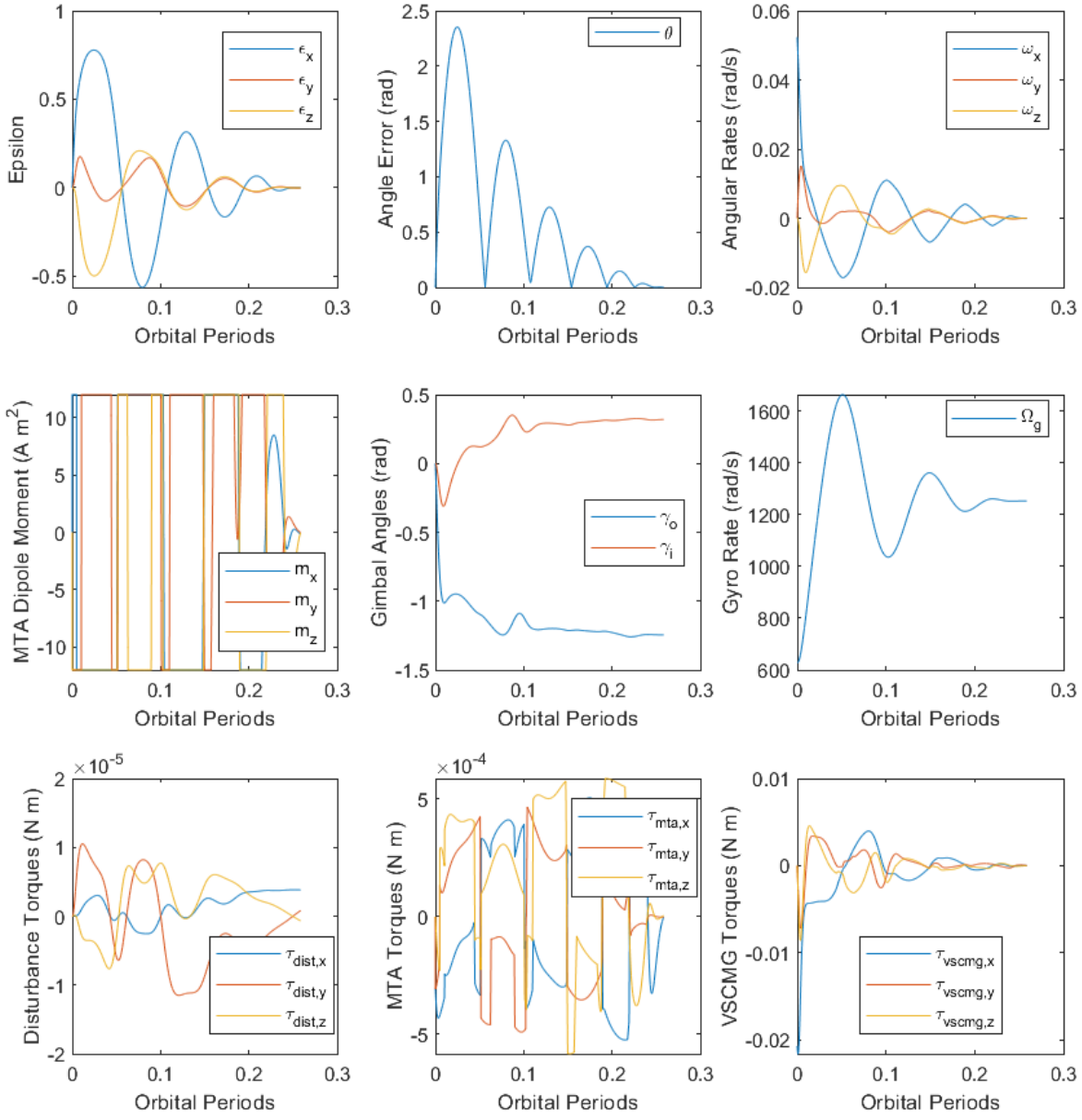

Figure 3.10: Simulation of PD-Controller Detumbling where $K_{c,d} = 10^0$, $K_{m,d} = 10^9$

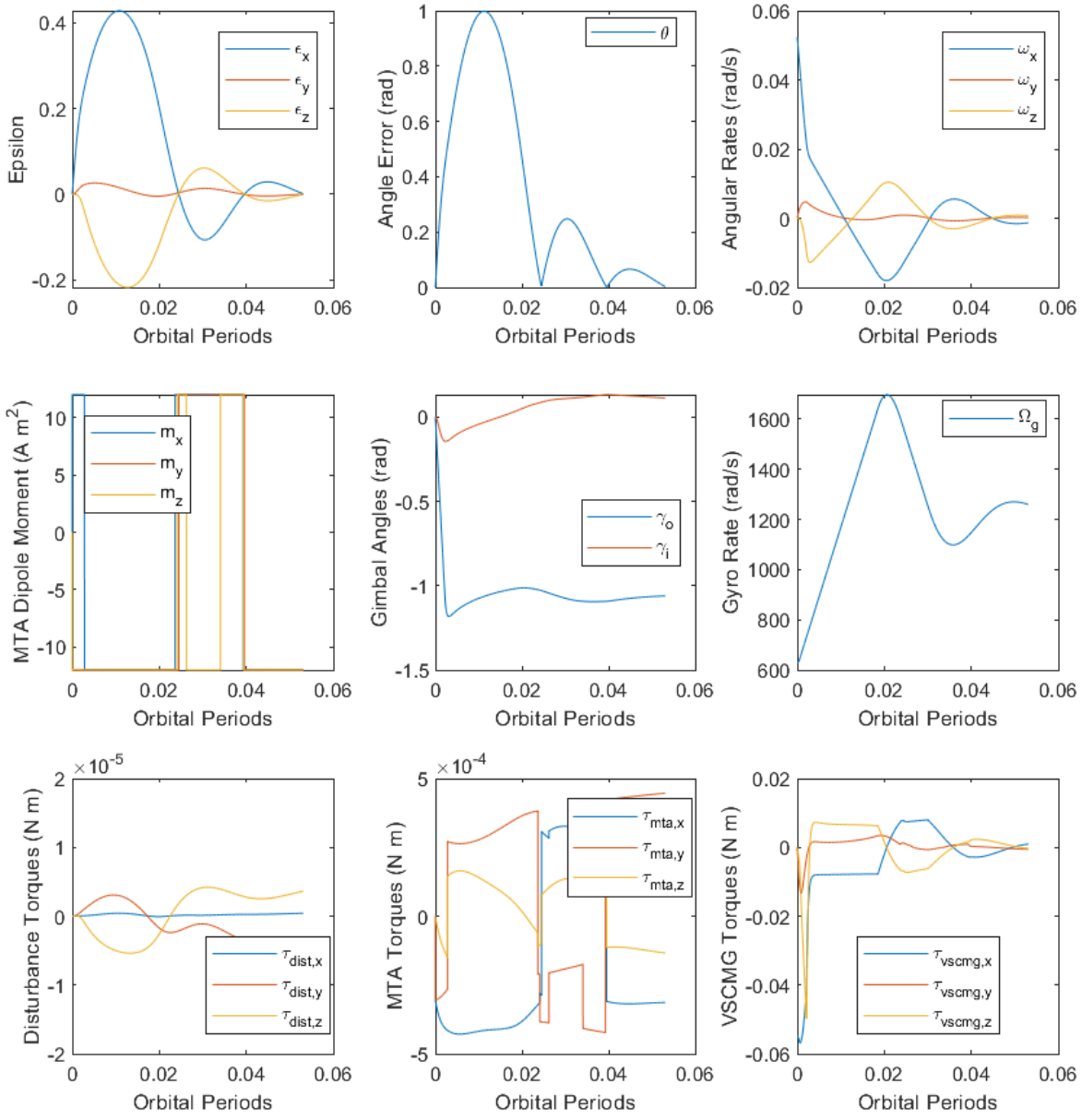

Figure 3.11: Simulation of PD-Controller Detumbling where $K_{c,d} = 10^1$, $K_{m,d} = 10^{10}$

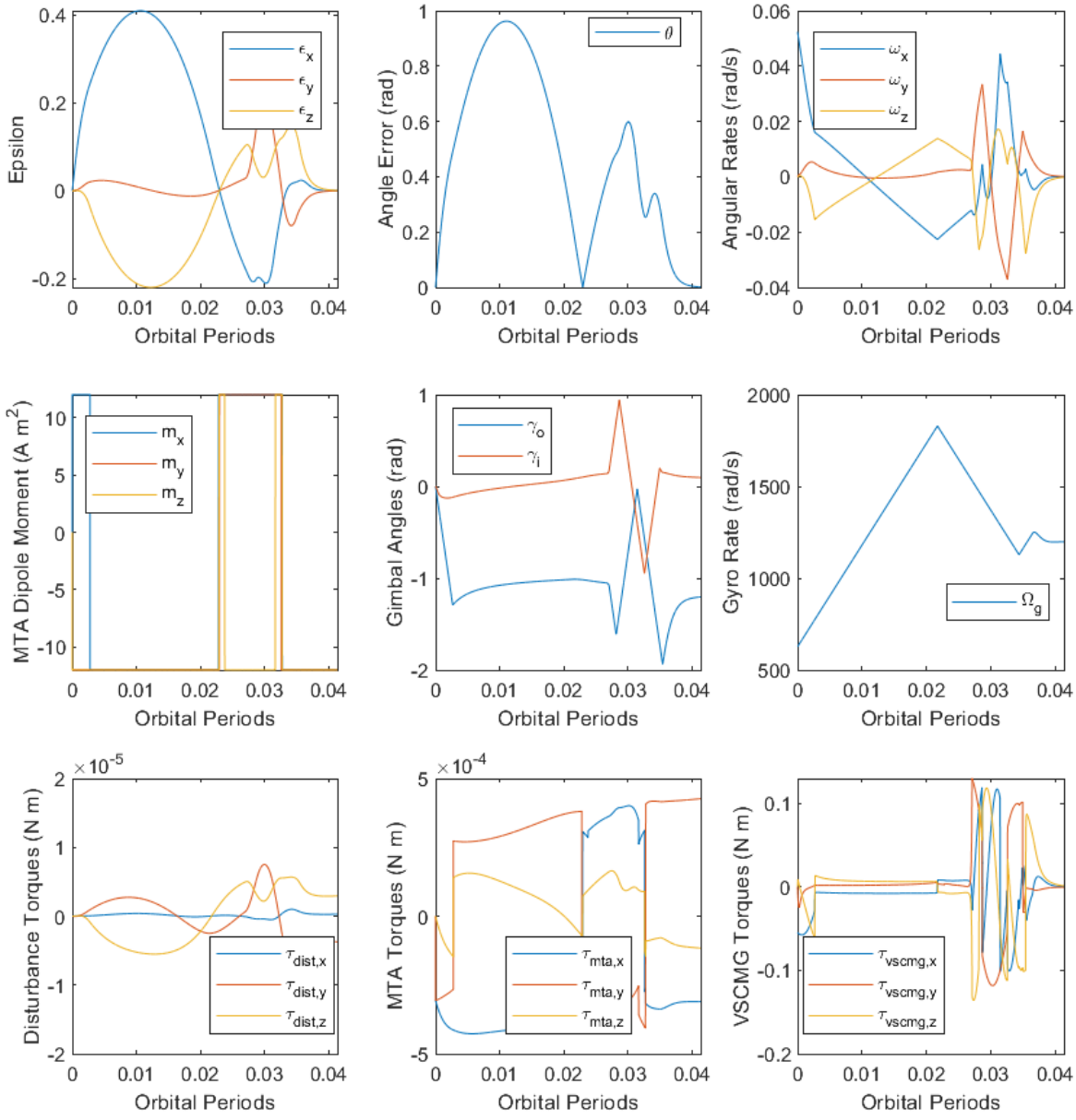

Figure 3.12: Simulation of PD-Controller Detumbling where $K_{c,d} = 10^2$, $K_{m,d} = 10^{11}$

Chapter 4

Linear Control

While manual and numerical tuning are the most accessible options for the nonlinear controller, linearizing the model and posing it as an LQR problem makes it possible to find an optimal controller. Because this is a highly nonlinear problem however, only the steady-state disturbance case is considered in this section; the detumbling case would very quickly leave the region where the linearized model is valid.

4.1 Linearization and LQR Optimization

The process for setting up an LQR problem is described in detail in Section 1.5. The state vector is $\boldsymbol{x} = \begin{bmatrix} \boldsymbol{\epsilon} & \boldsymbol{\omega} & \boldsymbol{c} \end{bmatrix}^T \in \mathbb{R}^{9\times 1}$ and the control vector is $\boldsymbol{u} = \begin{bmatrix} \dot{\boldsymbol{c}} & \boldsymbol{m} \end{bmatrix}^T \in \mathbb{R}^{6\times 1}$. Finding an optimal control matrix $\boldsymbol{K}$ such that $\boldsymbol{u} = -\boldsymbol{K}\boldsymbol{x}$ requires knowing four other matrices: state matrices $\boldsymbol{A} \in \mathbb{R}^{9\times 9}$ and $\boldsymbol{B} \in \mathbb{R}^{9\times 6}$ as in Equation 1.3a and cost matrices $\boldsymbol{Q} \in \mathbb{R}^{9\times 9}$ and $\boldsymbol{R} \in \mathbb{R}^{6\times 6}$ as in Equation 1.3b. The system when linearized about steady-state initial conditions has the following $\boldsymbol{A}$ and $\boldsymbol{B}$:

$$\boldsymbol{A} = \begin{bmatrix} 0 & 0 & 0 & \frac{1}{2} & 0 & 0 & 0 & 0 & 0 \\ 0 & 0 & 0 & 0 & \frac{1}{2} & 0 & 0 & 0 & 0 \\ 0 & 0 & 0 & 0 & 0 & \frac{1}{2} & 0 & 0 & 0 \\ 2.4237 \times 10^{-9} & 0 & 0 & 0 & -\frac{\pi}{105} & 0 & 0 & 0 & 0 \\ 0 & 1.8498 \times 10^{-6} & 0 & \frac{\pi}{125} & 0 & 0 & 0 & 0 & 0 \\ -1.8851 \times 10^{-9} & -1.8851 \times 10^{-9} & 1.1406 \times 10^{-6} & 0 & 0 & 0 & 0 & 0 & 0 \\ 0 & 0 & 0 & 0 & 0 & 0 & 0 & 0 & 0 \\ 0 & 0 & 0 & 0 & 0 & 0 & 0 & 0 & 0 \\ 0 & 0 & 0 & 0 & 0 & 0 & 0 & 0 & 0 \end{bmatrix} \tag{4.1}$$

$$\boldsymbol{B} = \begin{bmatrix} 0 & 0 & 0 & 0 & 0 & 0 \\ 0 & 0 & 0 & 0 & 0 & 0 \\ 0 & 0 & 0 & 0 & 0 & 0 \\ \frac{\pi}{105} & 0 & 0 & 0 & 1.2119 \times 10^{-6} & 0 \\ 0 & \frac{\pi}{125} & 0 & -1.0180 \times 10^{-6} & 0 & 0 \\ 0 & 0 & \frac{1}{27000} & 0 & 0 & 0 \\ 1 & 0 & 0 & 0 & 0 & 0 \\ 0 & 1 & 0 & 0 & 0 & 0 \\ 0 & 0 & 1 & 0 & 0 & 0 \end{bmatrix} \tag{4.2}$$

The only requirement on the $\boldsymbol{Q}$ and $\boldsymbol{R}$ matrices is that they be positive definite. This gives a large number of degrees of freedom at first, but simplifying assumptions can be made:

1. $\boldsymbol{Q}$ and $\boldsymbol{R}$ are diagonal matrices with positive elements. (DoF = 15)
2. The three components of $\boldsymbol{\epsilon}$, $\boldsymbol{\omega}$, and $\boldsymbol{m}$ have the same coefficients. (DoF = 9)
3. The two gimbal components of $\boldsymbol{c}$ and $\dot{\boldsymbol{c}}$ have the same coefficients. (DoF = 7)
4. For equal torque between the gimbal and gyro terms of $\boldsymbol{c}$ and $\dot{\boldsymbol{c}}$, the gimbal terms are first weighted by initial gyro rate Ω_g. On top of this, they are weighted by the range of motion available to each actuator. (DoF = 5)
5. For equal torque between the VSCMG and MTA terms of $\boldsymbol{u}$, $\boldsymbol{m}$ and $\dot{\boldsymbol{c}}$ are first weighted by I_g/B where B is the scalar magnitude of the magnetic field. On top of this, they are weighted by the range of motion available to each actuator. (DoF = 4)

From the magnetic field model in Equation 1.5, we can calculate the magnitude of magnetic field B as per Equation 4.3. Because we cannot have time-varying terms in our $\boldsymbol{Q}$ and $\boldsymbol{R}$ matrices, the value taken for B will be the average over a quarter orbit as calculated in Equation 4.4, where $E(k)$ is the complete elliptic integral of the second kind and $k = \sqrt{3}\sin(\phi)i$. For an inclination $\phi = 40°$, $E(k) \approx 2$.

$$B = \frac{B_0}{R^3}\sqrt{1 + 3\sin^2(nt)\sin^2(\phi)} \tag{4.3}$$

$$B_{avg} = \frac{2n}{\pi}\frac{B_0}{R^3}\int_0^{\frac{\pi}{2n}} \sqrt{1 + 3\sin^2(nt)\sin^2(\phi)} = \frac{2n}{\pi}\frac{B_0}{R^3}E\left(\sqrt{3}\sin(\phi)i\right) \approx \frac{4n}{\pi}\frac{B_0}{R^3} \tag{4.4}$$

This leaves us with four tunable terms: Q_ϵ, Q_ω, Q_c, and R_u. They form the $\boldsymbol{Q}$ and $\boldsymbol{R}$ matrices as follows:

$$\begin{aligned}\boldsymbol{Q} &= diag\left(\begin{bmatrix} Q_\epsilon & Q_\epsilon & Q_\epsilon & Q_\omega & Q_\omega & Q_\omega & \frac{Q_c\Omega_g}{\dot{\gamma}_{max}} & \frac{Q_c\Omega_g}{\dot{\gamma}_{max}} & \frac{Q_c}{\dot{\Omega}_{g,max}} \end{bmatrix}\right) \\ \boldsymbol{R} &= diag\left(R_u \begin{bmatrix} \frac{I_g\Omega_g}{\dot{\gamma}_{max}} & \frac{I_g\Omega_g}{\dot{\gamma}_{max}} & \frac{I_g}{\dot{\Omega}_{g,max}} & \frac{B_{avg}}{m_{max}} & \frac{B_{avg}}{m_{max}} & \frac{B_{avg}}{m_{max}} \end{bmatrix}\right)\end{aligned} \tag{4.5}$$

Running these matrices through Equation 1.3e, we obtain a solution X which is used to compute the control matrix $\boldsymbol{K}$. This controller can now either be plugged into the linearized system (see Equation 1.3f) or into the nonlinear system (Equation 4.6) to evaluate its performance. Because it is redundant given the control input regulation provided by $\boldsymbol{R}$ and contradicts the assumption of unbounded input $\boldsymbol{u}$ for LQR optimization, the rate limits are not enforced for the linear controller.

$$\dot{\boldsymbol{x}} = \begin{bmatrix} \dot{\boldsymbol{\epsilon}} \\ \dot{\boldsymbol{\omega}} \\ \dot{c} \end{bmatrix} = \begin{bmatrix} \frac{1}{2}\boldsymbol{\omega}\boldsymbol{q} \\ \boldsymbol{I}_{sat}^{-1}\left[-\begin{bmatrix}\boldsymbol{G} & -\boldsymbol{B}_b^\times\end{bmatrix}\boldsymbol{K}\boldsymbol{x} + \frac{3\mu}{R^5}\boldsymbol{p}_b^\times \boldsymbol{I}_{sat}\boldsymbol{p}_b + \boldsymbol{m}_{res}^\times \boldsymbol{B}_b - \boldsymbol{\omega}^\times\left(\boldsymbol{I}_{sat}\boldsymbol{\omega} + \boldsymbol{L}_{cmg}\right)\right] \\ -\begin{bmatrix}\boldsymbol{1} & \boldsymbol{0}\end{bmatrix}\boldsymbol{K}\boldsymbol{x} \end{bmatrix} \tag{4.6}$$

Note that in Equation 4.6, $\boldsymbol{1}$ is the 3×3 identity matrix and $\boldsymbol{0}$ is the 3×3 zero matrix.

We also note that the ratio between the $\boldsymbol{R}$ matrix coefficient on the VSCMG gimbal terms and the MTA terms (see Equation 4.7). This is a hint toward the order of magnitude difference between the gains on the MTAs and VSCMG: the order of magnitude difference of 9.4 between actuator effectiveness is fairly close to the order of magnitude difference of 9 between the D gains on the MTA and VSCMG at equal torque (see Section 3.3.1). Because this is also weighted by the range of motion on each actuator, magnitude differences will vary with different combinations of actuators, but this provides a useful start to finding the proper ratio of gains.

$$\frac{\frac{I_g\Omega_g}{\dot{\gamma}_{max}}}{\frac{B_{avg}}{m_{max}}} = \frac{I_g\Omega_g m_{max}\pi R^3}{\dot{\gamma}_{max} 4nB_0} \approx 10^{9.4} \tag{4.7}$$

4.2 Characterizing the Optimization Space

With the assumptions made in the last section, the number of free terms in the $\boldsymbol{Q}$ and $\boldsymbol{R}$ matrices has been narrowed down to four: weights for angular position error Q_ϵ, angular velocity error Q_ω, gimbal position error Q_c, and control input error R_u. Q_ϵ and Q_ω are somewhat analogous to the P and D gains and can be varied for similar effect. Q_c and R_u have a similar relationship, as the latter includes gimbal rates error. As there was a clear optimal ratio between the P and D gains found by fmincon in Section 3.3.1, it is possible for

a similar optimum to be found between Q_c and R_u assuming values for Q_ϵ and Q_ω.

Figure 4.1 was generated assuming $Q_\epsilon = 10^7$ and $Q_\omega = 10^5$. There is a clear minimum R_u for a given Q_c, visible as a valley on the plot.

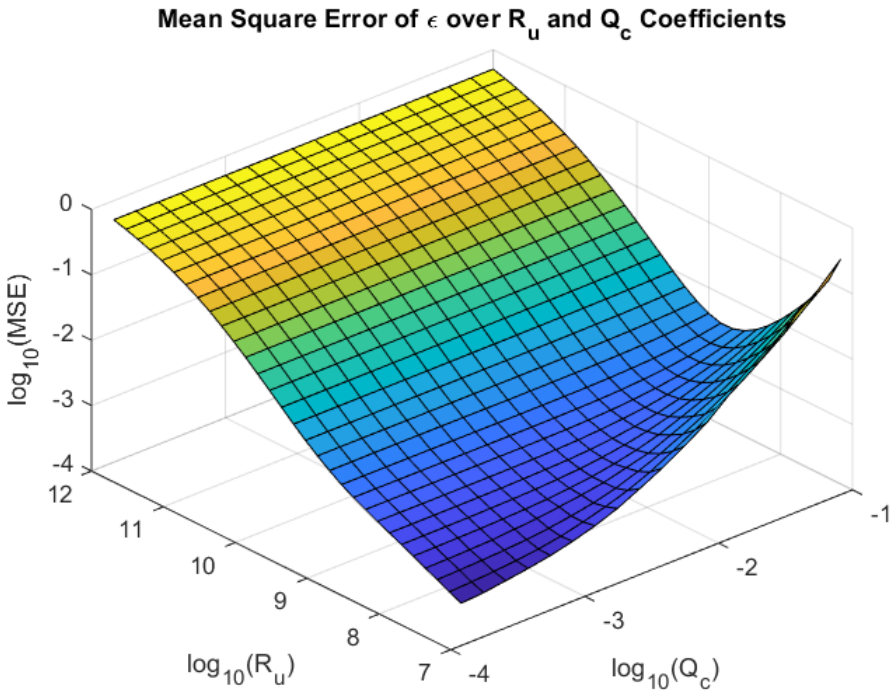

Figure 4.1: Mean Square Error over Q_c and R_u assuming $Q_\epsilon = 10^7$ and $Q_\omega = 10^5$

While Q_c technically weighs the state vector and R_u the control input, the fact that they are coupled through the VSCMG implies the optimal weighing that is visible in Figure 4.1. The monotonically decreasing error with Q_c is expected; a lower consideration of gimbal position error means a greater relative consideration of the spacecraft position error. Then given a particular Q_c, there must be an appropriate R_u to damp the VSCMG motion.

We can see this manifest in simulation. Consider the case where $Q_c = 10^{-2}$. The optimal $R_u \approx 10^{8.15}$. In the case where R_u is low ($R_u = 10^7$), we see in Figure 4.2 that the controller causes a lot of high frequency, high amplitude motion in the VSCMG, especially near the beginning. When R_u is high ($R_u = 10^{10}$), we see in Figure 4.3 that the motion of the VSCMG is much smoother and lower amplitude, but the angular position error reaches a much higher magnitude before corrective torque is applied. At the optimal value of $R_u = 10^{8.15}$, Figure 4.4 shows that the motion is smoother than in the low case while angular position error is corrected in a much shorter time than in the high case.

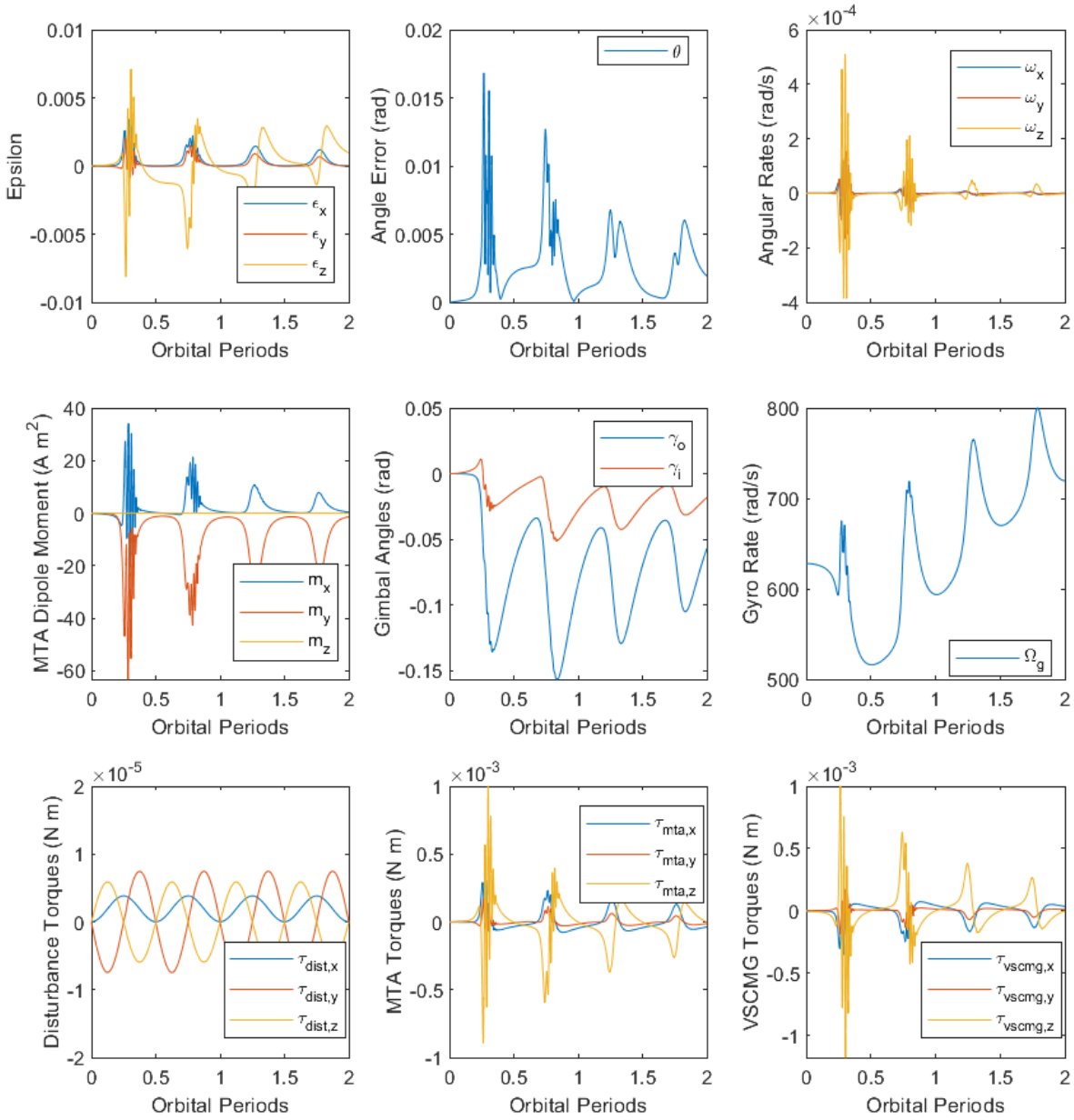

Figure 4.2: Simulation of Linear Controller where $Q_\epsilon = 10^7$, $Q_\omega = 10^5$, $Q_c = 10^{-2}$, and $R_u = 10^7$

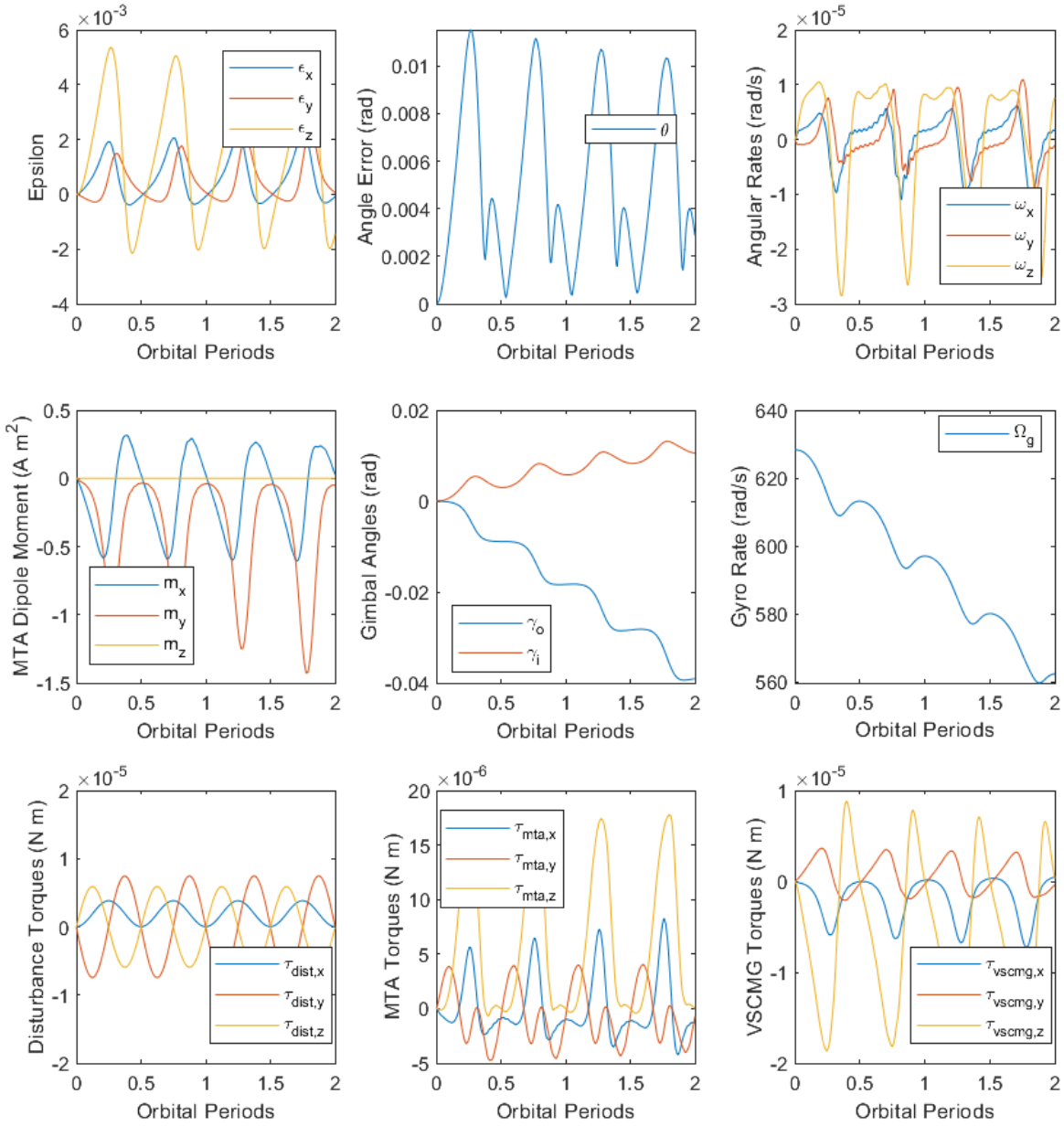

Figure 4.3: Simulation of Linear Controller where $Q_\epsilon = 10^7$, $Q_\omega = 10^5$, $Q_c = 10^{-2}$, and $R_u = 10^{10}$

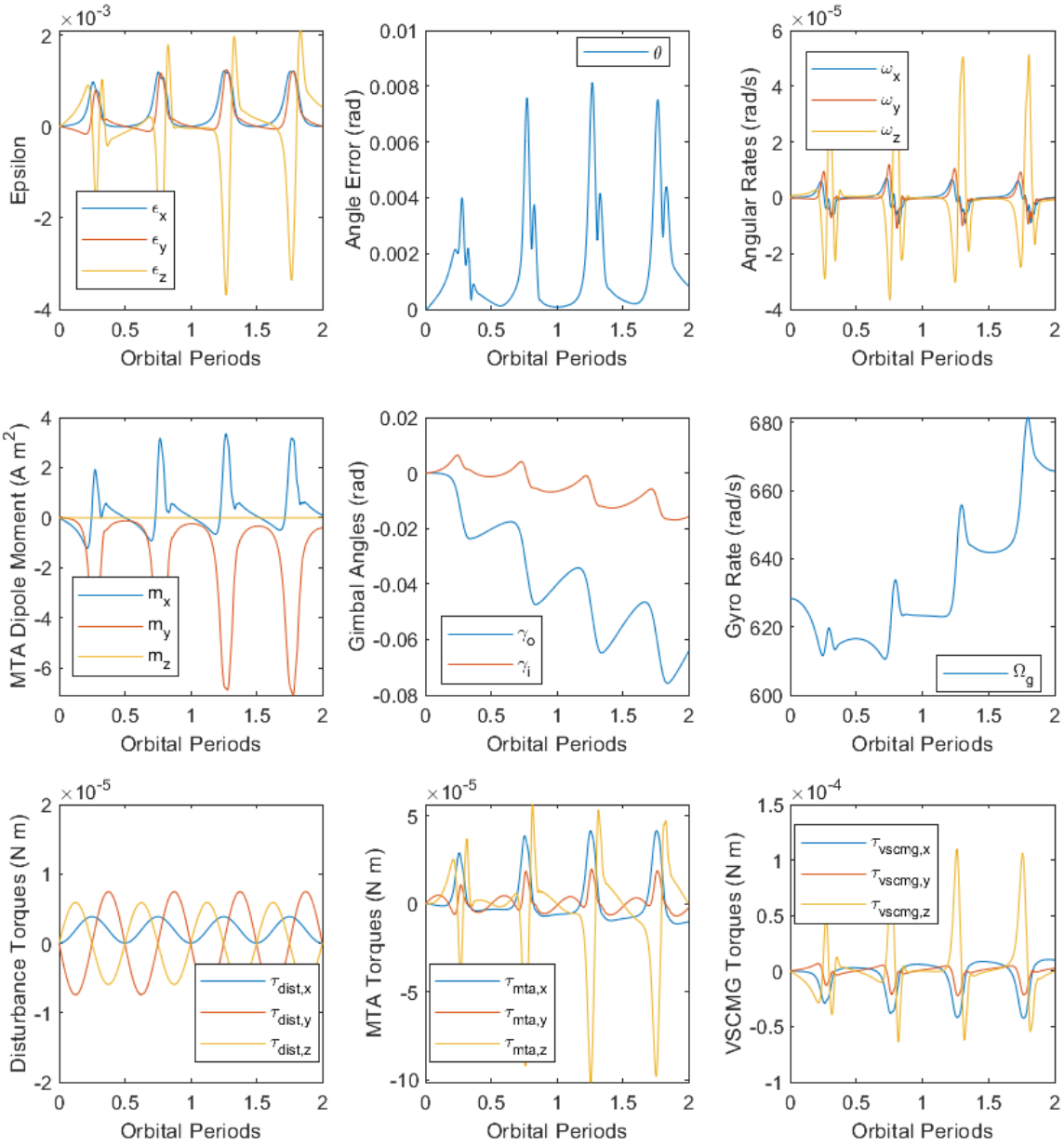

Figure 4.4: Simulation of Linear Controller where $Q_\epsilon = 10^7$, $Q_\omega = 10^5$, $Q_c = 10^{-2}$, and $R_u = 10^{8.15}$

Chapter 5

Limitations and Future Work

5.1 Spacecraft Design and Mission Considerations

In an effort to put the torques from the VSCMG and MTAs on similar orders of magnitude, the chosen specifications were for a relatively small VSCMG and relatively strong MTAs. This is intended to be useful for small spacecraft design, as the largest available MTAs are more readily usable on small spacecraft than the largest available CMGs, which are usable on spacecraft as large as the ISS.[10] It is intrinsic to the actuators' designs that the VSCMG will provide far more torque than the MTA. Future analysis of this actuator combination could consider designs that provide greater difference in magnitude between VSCMG and MTA torque.

The control inputs were assumed throughout this document to be exactly controllable. A higher fidelity model would take into account the physical effects that limit the control inputs. In particular, it would model the electromagnetic hysteresis on the MTAs, the servo controllers driving the VSCMG gimbal carriages, and the motor controller driving the gyroscope. A higher fidelity model may also model the angular momentum and applied torque from the gimbal carriages and from the gyroscope about all axes, but these are unlikely to be significant against the angular momentum and torque due to the sources considered in this thesis.

The scenarios considered in this thesis were single-purpose and extremely simple. Longer-term missions which require switching between different target angular positions and rates, different power consumption goals, etc. may lead to different compromise controllers, or more sophisticated control schemes than presented here. Future studies could consider the implications of, for example, tracking a distant moving target as though aiming a space telescope, maintaining a particular angular rate as though in a geosynchronous orbit, or explicitly incorporating VSCMG desaturation into the combined controller.

The orbit studied in this thesis was chosen to be relatively low altitude for higher usable magnetic field strength and moderate inclination to produce some variation in the magnetic field vector, which as previously discussed allows an MTA-equipped spacecraft to apply control torque about all three axes when spread over an orbit. The use of MTAs restricts a spacecraft of this configuration to Earth orbit, but the utility of a VSCMG has yet to be evaluated in-depth at the extremes of a polar/equatorial orbit or a highly elliptical orbit, which would lead to significant variation in magnetic field strength and direction.

5.2 Design Optimization Criteria

The evaluation criteria considered by this thesis were fairly straightforward. For the steady-state case, it was angular position mean square error over a relatively long time. For the detumbling case, it was convergence time, i.e. time from the simulation start to when angular velocity (and angular position if PD controller was used) became sufficiently small.

If power is in excess this is acceptable, but minimizing power consumption is usually desirable on small spacecraft where solar panel area and battery space are limited and thermonuclear generators are impractical. Making use of performance specifications to determine power consumption for given control inputs would allow power to be used as an optimization criterion. If this is weighted with a performance objective like mean square error, then it could be used to determine the most energy-efficient control schemes for a setup like this and contrast it with pure MTA or VSCMG systems.

For more sophisticated missions as discussed in the previous section, objectives may change. For example, a power-efficient controller may be used for the long-term segments where the spacecraft has to hold some angular position, but switch to a power-hungry controller when adjusting to a completely new position to minimize down-time. A study of common, planned, or desired missions for small spacecraft that may make use of this ACS setup would be useful to tailor objective criteria and design a more specific and optimal controller.

Conclusion

In this thesis I analyzed a proposed ACS consisting of a VSCMG and three orthogonal MTAs for small, Earth-orbiting spacecraft. I showed that such a system was precisely controllable to a level not achievable with an MTA system in long-term steady-state control. I also showed that in the detumbling case, the hybrid ACS is able to continue to reduce convergence time long after the MTA performance limits have been reached by using the excess of torque available from the VSCMG. I also demonstrated the functionality of a steady-state LQR controller simplified to only four degrees of freedom, despite the highly nonlinear nature of the spacecraft and ACS dynamics.

On top of demonstrating the promise of the hybrid system, the first steps have been made to characterizing its performance against the control inputs. In steady state, the effective region for the MTA D gain has been identified as a function of the VSCMG D gain and the factor by which it improves performance is consistent. The order of magnitude difference between the control gains is characterizable by the actuators' specifications and dynamics and is fairly close to the empirical values found. A minimal error relation between two of the free terms in the $\boldsymbol{Q}$ and $\boldsymbol{R}$ matrices was found, potentially reducing the degrees of freedom further to only three. And in detumbling, the D-controller system is shown to decelerate no matter the magnitude of gains, and the PD-controller system is shown to converge in the cases tested.

There are limitations that could be addressed by future research. Only one orbit, two scenarios, and one spacecraft were considered, and the empirical relations found in this thesis will almost certainly change with different specifications. The models for dynamics and control were fairly idealized and straightforward, not modelling hysteresis, lag, or backlash in electromechanical components in the physical hardware. A specific 'desaturation mode' could be implemented to bring the gimbal angles and gyro rate back to initial conditions when the MTAs are aligned properly with the magnetic field.

The extremely increased precision and convergence speed associated with this hybrid system opens the door to microsatellite missions that take advantage of these qualities. Low-cost geosynchronous microsatellites can stay focused on the same location with ground

position error on the order of metres. Low-cost space telescopes could use such a system to greatly reduce angular wobble as it takes long-exposure photographs. When changing targets, it would spend less time adjusting position and more time in operation. As a compromise between hardware complexity, size, and performance, the VSCMG/MTA system has the potential to make entire categories of mission far easier to design and accomplish.

Bibliography

[1] National Aeronautics and Space Administration. Space shuttle reaction control system, 2000. `http://science.ksc.nasa.gov/shuttle/technology/sts-newsref/sts-rcs.html`. Accessed 2019-01-26.

[2] Nazareth Bedrossian, Joseph Paradiso, Edward V. Bergmann, and Derek Rowell. Redundant single gimbal control moment gyroscope singularity analysis. *Journal of Guidance, Control, and Dynamics*, 13, 01 1991.

[3] W.B. Chubb, S.M. Seltzer, United States. National Aeronautics, Space Administration, and George C. Marshall Space Flight Center. *Skylab Attitude and Pointing Control System*. NASA technical note. National Aeronautics and Space Administration, 1971.

[4] A Craig Stickler and K.T. Alfriend. Elementary magnetic attitude control system. *Journal of Spacecraft and Rockets*, 13, 09 1974.

[5] CubeSatShop.com. Nctr-m002 magnetorquer rod, 2018. `https://www.cubesatshop.com/product/nctr-m002-magnetorquer-rod/`. Accessed 2018-10-14.

[6] A Dean Jacot and D J. Liska. Control moment gyros in attitude control. *Journal of Spacecraft and Rockets - J SPACECRAFT ROCKET*, 3:1313–1320, 09 1966.

[7] Stanford University EE363. Lecture 4 - continuous time linear quadratic regulator, 2008. `https://web.stanford.edu/class/ee363/lectures/clqr.pdf`. Accessed 2019-01-27.

[8] James Richard Forbes and Christopher John Damaren. Geometric approach to spacecraft attitude control using magnetic and mechanical actuation. *Journal of Guidance, Control, and Dynamics*, 33(2):590–595, 3 2010.

[9] Vincent Francois-Lavet. Study of passive and active attitude control systems for the oufti nanosatellites. 2010.

[10] Charles Gurrisi, Raymond Seidel, Scott Dickerson, Stephen Didziulis, Peter Frantz, and Kevin Ferguson. Space station control moment gyroscope lessons learned. 04 2019.

[11] Peter C Hughes. *Spacecraft Attitude Dynamics*. Dover Publications, 2012.

[12] Jaehyun Jin and Inseok Hwang. Attitude control of a spacecraft with single variable-speed control moment gyroscope. *Journal of Guidance, Control, and Dynamics*, 34:1920–1925, 11 2011.

[13] Vaios Lappas, Willem Steyn, and Craig Underwood. Design and testing of a control moment gyroscope cluster for small satellites. *Journal of Spacecraft and Rockets - J SPACECRAFT ROCKET*, 42:729–739, 07 2005.

[14] Marco Lovera and Alessandro Astolfi. Spacecraft attitude control using magnetic actuators. *Automatica*, 40:1405–1414, 08 2004.

[15] Makesat. Magnetic torquer for small satellites, 2016. `https://makesat.com/en/products/magnetic-torquer-for-satellites`. Accessed 2019-04-07.

[16] R. Miyagusuku, K. R. Arias, and E. R. Villota. Hybrid magnetic attitude control system under cubesat standards. In *2012 IEEE Aerospace Conference*, pages 1–9, March 2012.

[17] S R. Vadali, S R. Walker, and Hwa-Suk Oh. Preferred gimbal angles for single gimbal control moment gyros. *Journal of Guidance Control Dynamics*, 13:1090–1095, 11 1990.

[18] James Richard Forbes and Christopher John Damaren. Linear time-varying passivity-based attitude control employing magnetic and mechanical actuation. *Journal of Guidance, Control, and Dynamics*, 34, 08 2010.

[19] David J. Richie, Vaios J. Lappas, and George Prassinos. A practical small satellite variable-speed control moment gyroscope for combined energy storage and attitude control. *Acta Astronautica*, 65(11):1745 – 1764, 2009.

[20] Stanislav Ryaboukha, Ken Hrovat, Milton Miskowitz, and Rich Delombard. Further analysis of the microgravity environment on mir space station during mir-16. 07 1996.

[21] John S. White, Fred H. Shigemoto, and Kent Bourquin. Satellite attitude control utilizing the earth's magnetic field. 09 1961.

[22] V.A. Sarychev and V.V. Sazonov. Gravity gradient stabilization of the salyut-soyuz orbital complex. *Acta Astronautica*, 11(7):435 – 447, 1984.

[23] Enrico Silani and Marco Lovera. Magnetic spacecraft attitude control: a survey and some new results. *Control Engineering Practice*, 13(3):357 – 371, 2005. Aerospace IFAC 2002.

[24] Shu Tsujii, Mai Bando, and Hiroshi Yamakawa. Spacecraft formation flying dynamics and control using the geomagnetic lorentz force. *Journal of Guidance, Control, and Dynamics*, 36:136–148, 01 2013.

[25] Fiona Turett, United States. National Aeronautics, Space Administration, and Johnson Space Center. *Propellant Savings during Soyuz Undock from the International Space Station*. NASA technical note. National Aeronautics and Space Administration, 2016.

[26] Behrad Vatankhahghadim and Christopher John Damaren. Optimal combination of magnetic attitude control with impulsive thrusting. *Journal of Guidance, Control, and Dynamics*, 39(10):2391–2398, 10 2016.

[27] J. T. . Wen and K. Kreutz-Delgado. The attitude control problem. *IEEE Transactions on Automatic Control*, 36(10):1148–1162, Oct 1991.

[28] Rafal Wisniewski. Linear time varying approach to satellite attitude control using only electromagnetic actuation. *Journal of Guidance, Control, and Dynamics*, 23(4):640–647, 2000.

[29] Juan Zamorano, Jorge Garrido, Javier Cubas, Alejandro Alonso, and Juan A. de la Puente. The design and implementation of the upmsat-2 attitude control system. *IFAC-PapersOnLine*, 50(1):11245 – 11250, 2017. 20th IFAC World Congress.

Appendix A

Matlab Code

The simulation code for the proposed spacecraft was written in Matlab. The functions in this section were used to simulate the spacecraft dynamics with the linear controller and nonlinear controller in detumbling and steady-state scenarios. It can be found on Github at `https://github.com/ailersic/vscmg-mta-spacecraft`. If bugs are identified or improvements made to this code, the updated version can be found there.

A.1 vscmg_mt_dynamics.m

This function represents the basic dynamics equation $\dot{\boldsymbol{x}} = f(\boldsymbol{x}, \boldsymbol{u}, t)$ where $\boldsymbol{x}$ is the state vector, $\boldsymbol{u}$ is the input vector, and t is the current time. The function inputs are as follows:

x State vector $\boldsymbol{x}$ containing angular position $\boldsymbol{\epsilon}$, angular rates $\boldsymbol{\omega}$, and VSCMG state $\boldsymbol{c}$
u Control input $\boldsymbol{u}$ containing VSCMG rates $\dot{\boldsymbol{c}}$ and MTA dipole moments $\boldsymbol{m}$
t Current simulation time t
params Structure containing spacecraft and mission specifications, including moment of inertia matrix, orbital radius, etc.

And the outputs:

xdot Derivative of state vector $\dot{\boldsymbol{x}}$
cdot Derivative of gimbal state vector $\dot{\boldsymbol{c}}$
m MTA dipole moment $\boldsymbol{m}$
tau_mta Torque due to MTAs $\boldsymbol{\tau}_{mta}$
tau_vscmg Torque due to VSCMG $\boldsymbol{\tau}_{vscmg}$
tau_ggs Torque due to GGS $\boldsymbol{\tau}_{ggs}$
tau_magres Torque due to residual magnetic field $\boldsymbol{\tau}_{magres}$

```
function [xdot, cdot, m, tau_mta, tau_vscmg, tau_ggs, tau_magres] ...
    = vscmg_mt_dynamics(x, u, t, params)
    %% Read input

    eps = x(1:3, :);
    eta = real(sqrt(1 - sum(eps.^2, 1)));

    q = [eta; eps];
    w = x(4:6, :);
    c = x(7:9, :);

    cdot = u(1:3, :);
    m = u(4:6, :);

    nt = size(x, 2);

    %% Physical constants

    mu = 6.67e-11*5.972e24; % m^3/s^2
    B0 = -7.9e15; % Wb m

    %% Orbital position and magnetic field

    n = sqrt(mu/(params.R^3)); % 1/s
    p_i = params.R*[cos(n*t'); ...
                    sin(n*t')*cos(params.incl); ...
                    sin(n*t')*sin(params.incl)];
    B_i = B0/(params.R^5)*[3*p_i(1,:).*p_i(3,:); ...
                           3*p_i(2,:).*p_i(3,:); ...
                           2*p_i(3,:).^2 - p_i(1,:).^2 - p_i(2,:).^2];

    C_bi = zeros(3, 3, nt);
    p_b = zeros(3, nt);
    B_b = zeros(3, nt);

    for i=1:nt
```

```
        C_bi(:, :, i) = [q(1, i)^2 + q(2, i)^2 - q(3, i)^2 - q(4, i)^2, ...
                         2*q(2, i)*q(3, i) - 2*q(1, i)*q(4, i), ...
                         2*q(2, i)*q(4, i) + 2*q(1, i)*q(3, i); ...
                         2*q(2, i)*q(3, i) + 2*q(1, i)*q(4, i), ...
                         q(1, i)^2 - q(2, i)^2 + q(3, i)^2 - q(4, i)^2, ...
                         2*q(3, i)*q(4, i) - 2*q(1, i)*q(2, i); ...
                         2*q(2, i)*q(4, i) - 2*q(1, i)*q(3, i), ...
                         2*q(3, i)*q(4, i) + 2*q(1, i)*q(2, i), ...
                         q(1, i)^2 - q(2, i)^2 - q(3, i)^2 + q(4, i)^2];

        p_b(:, i) = C_bi(:, :, i)*p_i(:, i);
        B_b(:, i) = C_bi(:, :, i)*B_i(:, i);
    end

    %% VSCMG

    G = zeros(3, 3, nt);
    L_vscmg = zeros(3, nt);

    for i=1:nt
        G(:, :, i) = params.Icmg*[cos(c(1, i))*cos(c(2, i))*c(3, i), ...
                                  -sin(c(1, i))*sin(c(2, i))*c(3, i), ...
                                  sin(c(1, i))*cos(c(2, i));
                                  0, ...
                                  cos(c(2, i))*c(3, i), ...
                                  sin(c(2, i)); ...
                                  -sin(c(1, i))*cos(c(2, i))*c(3, i), ...
                                  -cos(c(1, i))*sin(c(2, i))*c(3, i), ...
                                  cos(c(1, i))*cos(c(2, i))];

        L_vscmg(:, i) = params.Icmg*[sin(c(1, i))*cos(c(2, i))*c(3, i); ...
                                     sin(c(2, i))*c(3, i); ...
                                     cos(c(1, i))*cos(c(2, i))*c(3, i)];
    end

    %% Rigid body dynamics
```

```
    tau_mta = zeros(3, nt);
    tau_vscmg = zeros(3, nt);
    tau_ggs = zeros(3, nt);
    tau_magres = zeros(3, nt);
    tau = zeros(3, nt);
    wdot = zeros(3, nt);

    for i=1:nt
        tau_mta(:, i) = cross(m(:, i), B_b(:, i));
        tau_vscmg(:, i) = G(:, :, i)*cdot(:, i);
        tau_ggs(:, i) = 3*mu/(params.R^5)*cross(p_b(:, i), ...
                                              params.Isat*p_b(:, i));
        tau_magres(:, i) = cross(params.mres, B_b(:, i));

        tau(:, i) = tau_mta(:, i) + tau_vscmg(:, i) + ...
                    tau_ggs(:, i) + tau_magres(:, i);
        wdot(:, i) = params.invIsat*(tau(:, i) - ...
                                     cross(w(:, i), ...
                                     params.Isat*w(:, i) + ...
                                     L_vscmg(:, i)));
    end

    %% Assemble xdot

    qdot = zeros(4, nt);

    for i=1:nt
        qdotq = 0.5*quaternion([0; w(:, i)]')*quaternion(q(:, i)');
        [qdot(1, i), qdot(2, i), qdot(3, i), qdot(4, i)] = parts(qdotq);
    end

    xdot = [qdot(2:4, :); wdot; cdot];
end
```

A.2 vscmg_mt_control.m

This function represents the nonlinear control laws detailed in the thesis body, of the form $\boldsymbol{u} = f(\boldsymbol{x}, t)$ where $\boldsymbol{x}$ is the state vector, $\boldsymbol{u}$ is the input vector, and t is the current time. The function inputs are as follows:

x State vector $\boldsymbol{x}$ containing angular position $\boldsymbol{\epsilon}$, angular rates $\boldsymbol{\omega}$, and VSCMG state $\boldsymbol{c}$

t Current simulation time t

K Vector of control gains $K_{c,d}$, $K_{m,d}$, $K_{c,p}$, and $K_{m,p}$

params Structure containing spacecraft and mission specifications, including moment of inertia matrix, orbital radius, etc.

And the output:

u Control input $\boldsymbol{u}$ containing VSCMG rates $\dot{\boldsymbol{c}}$ and MTA dipole moments $\boldsymbol{m}$

```
function u = vscmg_mt_control(x, t, K, params)
    %% Read input

    eps = x(1:3, :);
    eta = real(sqrt(1 - sum(eps.^2, 1)));

    q = [eta; eps];
    w = x(4:6, :);
    c = x(7:9, :);

    nt = size(x, 2);

    %% Parse control inputs

    KcD = K(1);
    KmD = K(2);
    KcP = K(3);
    KmP = K(4);

    %% Physical constants

    mu = 6.67e-11*5.972e24; % m^3/s^2
```

```
B0 = -7.9e15; % Wb m

%% Orbital position and magnetic field

n = sqrt(mu/(params.R^3)); % 1/s
p_i = params.R*[cos(n*t'); ...
                sin(n*t')*cos(params.incl); ...
                sin(n*t')*sin(params.incl)];
B_i = B0/(params.R^5)*[3*p_i(1,:).*p_i(3,:); ...
                       3*p_i(2,:).*p_i(3,:); ...
                       2*p_i(3,:).^2 - p_i(1,:).^2 - p_i(2,:).^2];

C_bi = zeros(3, 3, nt);
p_b = zeros(3, nt);
B_b = zeros(3, nt);

for i=1:nt
    C_bi(:, :, i) = [q(1, i)^2 + q(2, i)^2 - q(3, i)^2 - q(4, i)^2, ...
                     2*q(2, i)*q(3, i) - 2*q(1, i)*q(4, i), ...
                     2*q(2, i)*q(4, i) + 2*q(1, i)*q(3, i); ...
                     2*q(2, i)*q(3, i) + 2*q(1, i)*q(4, i), ...
                     q(1, i)^2 - q(2, i)^2 + q(3, i)^2 - q(4, i)^2, ...
                     2*q(3, i)*q(4, i) - 2*q(1, i)*q(2, i); ...
                     2*q(2, i)*q(4, i) - 2*q(1, i)*q(3, i), ...
                     2*q(3, i)*q(4, i) + 2*q(1, i)*q(2, i), ...
                     q(1, i)^2 - q(2, i)^2 - q(3, i)^2 + q(4, i)^2];

    p_b(:, i) = C_bi(:, :, i)*p_i(:, i);
    B_b(:, i) = C_bi(:, :, i)*B_i(:, i);
end

%% VSCMG

G = zeros(3, 3, nt);

for i=1:nt
```

```
        G(:, :, i) = params.Icmg*[cos(c(1, i))*cos(c(2, i))*c(3, i), ...
                                  -sin(c(1, i))*sin(c(2, i))*c(3, i), ...
                                  sin(c(1, i))*cos(c(2, i)); ...
                                  0, ...
                                  cos(c(2, i))*c(3, i), ...
                                  sin(c(2, i)); ...
                                  -sin(c(1, i))*cos(c(2, i))*c(3, i), ...
                                  -cos(c(1, i))*sin(c(2, i))*c(3, i), ...
                                  cos(c(1, i))*cos(c(2, i))];
    end

    %% Calculate control inputs

    KcD = diag([KcD, ...
                KcD, ...
                KcD*params.x0(9)*params.cdotmax(3)/params.cdotmax(1)]);
    KcP = diag([KcP, ...
                KcP, ...
                KcP*params.x0(9)*params.cdotmax(3)/params.cdotmax(1)]);

    cdot = zeros(3, nt);
    m = zeros(3, nt);

    for i=1:nt
        cdot(:, i) = -KcD*G(:, :, i)'*w(:, i) - KcP*G(:, :, i)'*eps(:, i);
        m(:, i) = -KmD*cross(B_b(:, i), w(:, i)) - ...
                    KmP*cross(B_b(:, i), eps(:, i));
        for j=1:3
            cdot(j, i) = max(min(cdot(j, i), params.cdotmax(j)), ...
                             params.cdotmin(j));
            m(j, i) = max(min(m(j, i), params.mmax(j)), params.mmin(j));
        end
    end

    u = [cdot; m];
end
```

A.3 vscmg_mt_linearization.m

This function linearizes the dynamics given by `vscmg_mt_dynamics.m` and produces the matrices $\boldsymbol{A}$ and $\boldsymbol{B}$ to produce linearized equations of the form $\dot{\boldsymbol{x}} = \boldsymbol{A}\boldsymbol{x} + \boldsymbol{B}\boldsymbol{u}$ where $\boldsymbol{x}$ is the state vector and $\boldsymbol{u}$ is the input vector. It then uses the cost matrices $\boldsymbol{Q}$ and $\boldsymbol{R}$ to calculate the optimized control matrix $\boldsymbol{K}$. The function inputs are as follows:

Q Cost matrix $\boldsymbol{Q}$ that regulates the state vector $\boldsymbol{x}$

R Cost matrix $\boldsymbol{R}$ that regulates the control vector $\boldsymbol{u}$

params Structure containing spacecraft and mission specifications, including moment of inertia matrix, orbital radius, etc.

And the output:

K Optimized control matrix $\boldsymbol{K}$ that is used to calculate the control input $\boldsymbol{u} = \boldsymbol{K}\boldsymbol{x}$

A Linearized dynamics matrix $\boldsymbol{A}$

B Linearized dynamics matrix $\boldsymbol{B}$

```
function [K, A, B] = vscmg_mt_linearization(Q, R, params)
    %% Linearize system

    dx = 1e-6;
    du = 1e-6;

    A = zeros(length(params.x0), length(params.x0));
    B = zeros(length(params.x0), length(params.u0));

    for i=1:length(params.x0)
        dx0 = [zeros(i-1, 1); dx; zeros(length(params.x0)-i, 1)];
        A(:, i) = (vscmg_mt_dynamics(params.x0+dx0, params.u0, 0, ...
                                     params) - ...
                   vscmg_mt_dynamics(params.x0-dx0, params.u0, 0, ...
                                     params))/(2*dx);
    end

    for i=1:length(params.u0)
        du0 = [zeros(i-1, 1); du; zeros(length(params.u0)-i, 1)];
        B(:, i) = (vscmg_mt_dynamics(params.x0, params.u0+du0, 0, ...
```

```
                                    params) - ...
                    vscmg_mt_dynamics(params.x0, params.u0-du0, 0, ...
                                    params))/(2*du);
    end

    %% Check controllability

    if rank(ctrb(A, B)) == length(params.x0)
        disp('Controllable!')
    else
        disp('Not controllable!')
    end

    %% LQR Matrices and Riccati

    N = zeros(length(params.x0), length(params.u0));

    if min(eig([Q, N; N', R])) <= 0
        disp('Not solvable!')
    end

    K = -lqr(A, B, Q, R, N);
end
```

A.4 vscmg_mt_sim.m

Simulates the spacecraft dynamics using the nonlinear controller until the final simulation time is reached, at which point it integrates the square of position error over the entire time history and returns that as the controller error. It is intended to be used with steady-state simulations. The function inputs are as follows:

K Vector of control gains $K_{c,d}$, $K_{m,d}$, $K_{c,p}$, and $K_{m,p}$

params Structure containing spacecraft and mission specifications, including moment of inertia matrix, orbital radius, etc.

And the output:

err Integral of square of position error over entire time history

```
function err = vscmg_mt_sim(K, params)
    %% Simulate case

    options = odeset('RelTol',1e-5);
    [tsol, xsol] = ode15s(@(t, x) vscmg_mt_dynamics(x, ...
        vscmg_mt_control(x, t, K, params), t, params), [0, params.tf], ...
        params.x0, options);

    %% Calculate error

    eps = xsol(:, 1:3);
    err = sum(trapz(tsol, eps.^2));
end
```

A.5 vscmg_mt_sim_detumble.m

Simulates the spacecraft dynamics using the nonlinear controller until the final simulation time is reached, at which point it attempts to find the time taken until all control inputs and error terms converge within `tol` of zero. This convergence time is returned as the controller error. It is intended to be used with detumbling simulations. The function inputs are as follows:

K Vector of control gains $K_{c,d}$, $K_{m,d}$, $K_{c,p}$, and $K_{m,p}$

params Structure containing spacecraft and mission specifications, including moment of inertia matrix, orbital radius, etc.

And the output:

convtime Time until all control inputs and error terms converge to within `tol`

```
function convtime = vscmg_mt_sim_detumble(K, params)
    %% Simulate case

    options = odeset('RelTol',1e-5);
    [tsol, xsol] = ode15s(@(t, x) vscmg_mt_dynamics(x, ...
        vscmg_mt_control(x, t, K, params), t, params), [0, params.tf], ...
        params.x0, options);
    usol = vscmg_mt_control(xsol', tsol, K, params)';
```

```
    %% Calculate convergence time

    tol = 1e-3;
    isol = [];

    for i=1:length(tsol)
        if all(xsol(i, 1:6) < tol*ones(1, 6)) && all(usol(i, :) < ...
                tol*ones(1, 6))
            isol = i;
            break;
        end
    end

    if isempty(isol)
        convtime = params.tf;
    else
        convtime = tsol(isol);
    end
end
```

A.6 vscmg_mt_sim_lin.m

Simulates the spacecraft dynamics using the linear controller until the final simulation time is reached, at which point it integrates the square of position error over the entire time history and returns that as the controller error. It is intended to be used with steady-state simulations. The commented-out code is to simulate with the linearized dynamics for debugging purposes; this was not used for controller evaluation at any point in this thesis. The function inputs are as follows:

K Control matrix $\boldsymbol{K}$ that is used to calculate the control input $\boldsymbol{u} = \boldsymbol{K}\boldsymbol{x}$

params Structure containing spacecraft and mission specifications, including moment of inertia matrix, orbital radius, etc.

And the output:

err Integral of square of position error over entire time history

```
function err = vscmg_mt_sim_lin(K, params)
    %% Simulate case either with linearized or full dynamics

    %[~, A, B] = vscmg_mt_linearization(eye(9), eye(6), params);
    %[tsol, xsol] = ode15s(@(t, x) (A + B*K)*(x - params.x0), ...
    %                      [0, params.tf], params.x0);
    [tsol, xsol] = ode15s(@(t, x) vscmg_mt_dynamics(x, ...
                K*(x - params.x0), t, params), [0, params.tf], params.x0);

    %% Calculate error

    eps = xsol(:, 1:3);
    err = sum(trapz(tsol, eps.^2));
end
```